Washington University in St. Louis
Washington University Open Scholarship

Engineering and Applied Science Theses & Dissertations | McKelvey School of Engineering

Spring 5-2020

CFD modeling of Vertical Axis Wind Turbine Arrays using Actuator Cylinder Theory

Cory Schovanec

Follow this and additional works at: https://openscholarship.wustl.edu/eng_etds

 Part of the Aerodynamics and Fluid Mechanics Commons

Recommended Citation

Schovanec, Cory, "CFD modeling of Vertical Axis Wind Turbine Arrays using Actuator Cylinder Theory" (2020). *Engineering and Applied Science Theses & Dissertations*. 532.
https://openscholarship.wustl.edu/eng_etds/532

This Thesis is brought to you for free and open access by the McKelvey School of Engineering at Washington University Open Scholarship. It has been accepted for inclusion in Engineering and Applied Science Theses & Dissertations by an authorized administrator of Washington University Open Scholarship. For more information, please contact digital@wumail.wustl.edu.

Washington University in St. Louis

James McKelvey School of Engineering

Department of Mechanical Engineering & Material Science

Thesis Examination Committee:

Dr. Ramesh Agarwal, Chair

Dr. Swami Karunamoorthy

Dr. David Peters

CFD modeling of Vertical Axis Wind Turbine Arrays using Actuator Cylinder Theory

By

Cory Schovanec

A thesis presented to the James McKelvey School of Engineering of Washington University in St. Louis in partial fulfillment of the requirements for the degree of Master of Science

May 2020

St. Louis, Missouri

© 2020 Cory Schovanec

Dedication

This work is dedicated to my parents, Lawrence and Patty Schovanec. Thank you for the endless support and encouragement throughout all of my years of school.

Acknowledgements

I would like to thank the NASA-Missouri Space Consortium for supporting this research. I would also like to show my appreciation to all of the members of the CFD Laboratory at Washington University in St. Louis for taking the time to answer questions and provide insight throughout this process. The Engineering IT department was a great help; particularly, I would like to thank Allen Rueter and Gene Bulfin.

Most of all, I would like to express my deep gratitude to Dr. Agarwal, my research supervisor. This research would not have been possible without his support, guidance, and willingness to dedicate so much of his time to myself and all of his students.

Cory Schovanec

Washington University in St. Louis

May 2020

Table of Contents

List of Tables

List of Figures

Abstract

CFD modeling of Vertical Axis Wind Turbine Arrays using Actuator Cylinder Theory

By

Cory Schovanec

Master of Science in Aerospace Engineering

Washington University in St. Louis, Year

Research Advisor: Dr. Ramesh K. Agarwal

The goal of this thesis is to analyze the flow field and power generation from a vertical axis wind turbine (VAWT) by extending the Actuator Cylinder Model to include the viscous effects. Turbulent flow effects in the Actuator Cylinder Model are modeled by solving the Reynolds-Averaged Navier-Stokes (RANS) equations with the Spalart-Allmaras (SA) turbulence model in ANSYS FLUENT. A study is performed to establish mesh independence of the solutions. Numerical solutions on a fine mesh are compared to existing theoretical results based on inviscid theory for a series of flow conditions and turbine sizes. Similar trends in the present turbulent flow results are found as in the inviscid results for downstream velocity and pressure profiles. The Betz limit is found not to be applicable to vertical axis wind turbines. To consider wake interactions, the Actuator Cylinder Model is extended to two and three turbine cases. Power densities are computed to determine the optimal vertical and downstream distances between turbines. For the application to small scale airborne turbines, an increased freestream velocity is employed with two and three turbine models to simulate the effects on performance and power generation at higher altitudes with greater wind velocity. Differences between the present numerical results and inviscid theory are discussed.

Nomenclature

a = axial induction factor

A = rotor area

A_c = cross sectional area

c = chord length

C_D = rotor drag coefficient

Cp = rotor power coefficient

F_D = total drag force on cylinder

G_v = generation of turbulent viscosity

D = diameter of actuator cylinder

H = blade height

HAWT = horizontal axis wind turbine

m = pressure jump exponent

N = number of blades

Δp = pressure jump

P = converted power

R = radius

RANS = Reynolds Averaged Navier-Stokes

s = turbine spacing

SA = Spalart-Allmaras turbulence model

T = thrust

ρ = density of air

VAWT = vertical axis wind turbine

v_r = radial velocity

v_x = x component of velocity

v_y = ascent velocity

V_∞ = freestream velocity

$\tilde{v}$ = turbulent kinematic viscosity

W = weight due to gravity

Y_v = destruction of turbulent viscosity

x_{DF} = downfield distance of turbine in three VAWT array

Chapter 1: Introduction

1.1 Background

International Energy Agency (IEA) projects that the total capacity of renewables will increase by approximately 1.22 TW between 2020 and 2024 [1]. This includes a large role for wind energy; the capacity of the global wind fleet is expected to grow by over 60% during this time. This expansion can be attributed to a number of factors including the sustainable nature of wind energy, improved levels of cost-effectiveness, and the advancement of wind turbine technology. The primary focus of this research is the technical development of wind energy; this includes the emergence of new wind energy applications for vertical axis wind turbines, as well as alternate methods of wind energy analysis using computational fluid dynamics.

The design of wind turbines has evolved substantially since they were first introduced as a means to generate electricity in the late 1800s [2]. A number of different design parameters and configurations have been tested in order to optimize performance. One major parameter is the orientation at which the blades rotate. The two main classifications are vertical axis wind turbines (VAWT) and horizontal axis wind turbines (HAWT). Between the two, horizontal axis wind turbines are much more prevalent in modern design.

For a horizontal axis wind turbine (HAWT), the rotor axis is parallel to the ground or the wind direction. This is shown below in Fig. 1. The remaining parameters, such as the tower height, blade shape, and the number of blades, all may vary.

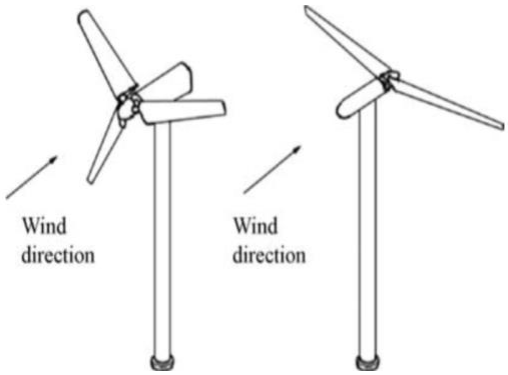

Figure 1. Schematic of Horizontal Axis Wind Turbine (HAWT) [2]

A big reason horizontal axis wind turbines (HAWT) have become more common than their vertical counterpart is a higher level of efficiency. When properly aligned with the wind, HAWTs can achieve efficiency up to 45% [2]. Comparatively, the typical efficiency of a VAWT is below 40% with a number of designs achieving 20% or less [3]. However, HAWTs are directionally dependent. This means that a yaw mechanism is required in order to keep the rotor perpendicular to the wind direction. In the case that the wind changes direction frequently, the yaw mechanism often fails to adjust in time and losses in power occur. Furthermore, this consideration also fails to account for the required land area. HAWTs produce large wakes that can significantly affect the performance of downfield turbines. For traditional HAWT arrays, a distance of 3-5 times the rotor diameter is required between vertically aligned HAWTs and a distance of 6-10 times the rotor diameter is required between downfield rows of HAWTs [4, 5]. As the average diameter is now up to 100m for onshore turbines, it is important that land area be considered jointly with efficiency [6].

For vertical axis wind turbines (VAWT), the rotor axis is perpendicular to the ground rather than the wind. One primary advantage of this design is that the directional dependence is eliminated; the turbines are always optimally aligned with the wind due to their angular symmetry. This means that a yaw mechanism is not required. In recent years, research has also

suggested that VAWTs may be aligned much closer to each other and thus achieve a higher power density. In fact, not only is it possible to reduce losses for downfield turbines, but when properly aligned downfield VAWTs may actually see an increase in performance [7]. This has made them a strong candidate for both extended array and small-scale applications where space is limited.

The purpose of this research is to further explore this phenomenon using the Actuator Cylinder Model. It should be noted, however, that the behavior of VAWTs is heavily dependent on the blade geometry. Some common variations are shown below.

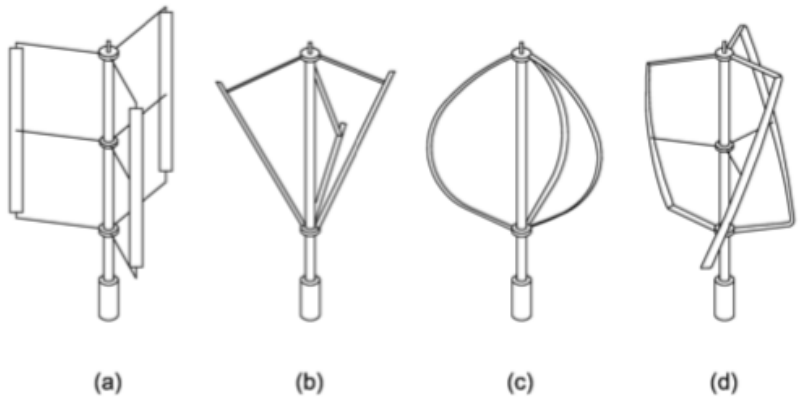

Figure 2. Schematic of Vertical Axis Wind Turbines (VAWT) [8]

The Actuator Cylinder Model is based on a straight bladed H-Type VAWT; as such, the focus of this thesis will be limited to turbines with the type (a) in Fig. 2 above.

1.2 Background Theory

With the expanding need for renewable wind power, there has been a need for simple but accurate wind turbine models to evaluate their aerodynamic performance for industrial applications. Since the seventies, several aerodynamic models have been developed for both horizontal axis wind turbines (HAWT) and vertical axis wind turbines (VAWT). Over the years, these models have become increasingly complex with the implementation of advanced CFD

techniques and the availability of high-performance computing platforms. While detailed CFD analysis may be required in some cases, it can often be advantageous to use a simplified model as long as the desired results still accurately represent the system [9, 10].

1.3 One-Dimensional Momentum Theory

One example of a simple aerodynamic model used for wind turbine analysis is the 1-D Momentum theory. This model, commonly referred to as the Actuator Disk Theory, utilizes an infinitely thin pressure jump within a stream tube surrounding the turbine. At the location of the actuator disk, it is assumed that the turbine has an infinite number of blades and that the resulting thrust is uniform [10].

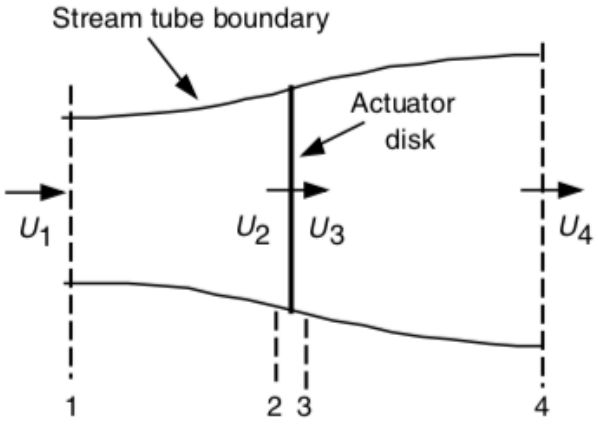

Figure 3. Schematic of Actuator Disk [10]

By applying the principles of conservation of mass and momentum, the power and flow field characteristics for an ideal HAWT can be obtained. Power is defined using the freestream velocity, which is denoted as U_1 in the figure above.

$$P = \frac{1}{2} \cdot \rho \cdot A \cdot U_1^3 \cdot 4a \cdot (1 - a)^2 \quad (1)$$

In Eq. 1, a is the axial induction factor which represents the fractional decrease in wind velocity between points 1 and 2. To characterize performance, the power coefficient C_p can then be calculated as the ratio of the calculated power to the theoretically possible power from the wind.

$$C_p = \frac{P}{\frac{1}{2}\cdot\rho\cdot V_\infty^3\cdot \mathrm{A}} \tag{2}$$

By combining Eq. 1 and 2 above, the power coefficient can be written in terms of the axial induction factor.

$$C_p = 4 \cdot a \cdot (1-a)^2 \tag{3}$$

The critical point $C_{p,max}$ can be calculated as $\frac{dC_p}{da} = 0$. From this process, it can be determined that the maximum power output corresponds to $a = 1/3$ and $C_p = 16/27$. This result, which is known as the Betz Limit, has been widely accepted as the theoretical maximum efficiency for a HAWT [10].

1.4 Actuator Cylinder Theory

While 1D Momentum Theory is still used today, alternative actuator disk models have been developed to overcome some of the original model's limitations, such as a non-rotating wake. Furthermore, while the model shown in Fig. 3 has had success with traditional horizontal axis wind turbines (HAWT), it is not an accurate representation of a VAWT. This was addressed by Heldge Madsen in his 1982 publication titled, "The Actuator Cylinder – A Flow Model for Vertical Axis Wind Turbines" [11]. In this thesis, the traditional actuator disk is replaced by a thin circular cylinder (Actuator Cylinder) that follows the blade path of a VAWT across which a pressure jump condition is applied. Similar to Actuator Disk Theory, the pressure jump is modeled for an ideal turbine; the number of blades and angular velocity are taken to approach infinity while the chord length of the blade approaches zero.

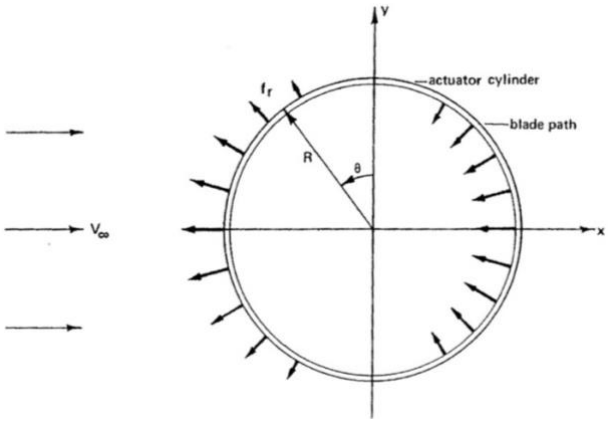

Figure 4. Schematic of Actuator Cylinder [11]

Using the actuator cylinder geometry shown in Fig. 4, analytical solutions for the induced velocities and pressure field were derived by Madsen using the Euler equations [11]. In the numerical model, the pressure jump has the form:

$$\Delta p(\theta) = \Delta p_{max} \frac{\sin(\theta)}{|\sin(\theta)|}(1 - |\cos(\theta)|^m + \frac{1}{2\pi}\sin(2\pi|\cos(\theta)|^m)) \tag{4}$$

where Δp_{max} is defined using the drag force, F_D. For a known drag coefficient C_D, and freestream velocity V_∞, Δp_{max} can be easily calculated using the following equation:

$$\Delta p_{max} = \frac{F_D}{2R} = \frac{1}{2} \cdot C_D \cdot \rho \cdot V_\infty^2 \tag{5}$$

For $\Delta p(\theta)$, the angle is defined from the positive *y*-axis and the exponent *m* is a constant. As *m* increases, the load form associated with the pressure jump becomes increasingly uniform and the solution to the actuator cylinder approaches that of the actuator disk [11].

To analyze the performance of the VAWT, the power per unit length of the rotor can be determined as:

$$P = \int_0^{2\pi} v_r \cdot \Delta p(\theta) \cdot R \cdot d\theta \tag{6}$$

where v_r is the radial velocity at the exterior of the cylinder. For discrete analysis, the power can be estimated using a Riemann sum as follows:

$$\sum_{i=1}^{i=n} v_{r,i} \cdot \Delta p_i \cdot R \cdot \Delta\theta \quad (7)$$

The power coefficient can once more be calculated using Eq. 2. For the actuator cylinder, the area A represents the swept area of the turbine. Since the analysis is restricted to the x-y plane, the swept area is simply equal to the rotor diameter. For more robust 3D analysis, the blade height would need to be modeled as well. For a finite blade height there would be tip losses at the upper and lower surfaces of the VAWT.

Chapter 2: Singe Actuator Cylinder Models

2.1 Physical Model and Grid

For comparison with inviscid theory, the computational domain was chosen to be identical to the domain of the largest and most refined mesh from Madsen [11]. The domain is rectangular with a length of 13m and a height of 8m. As shown in Fig. 5, the actuator cylinder is centered about the origin with a diameter of 2m. The entire domain is modeled with fluid medium as air. The density was 1.225 kg/m3 and the viscosity was $1.7894 \cdot 10^{-4}$ kg/m-s.

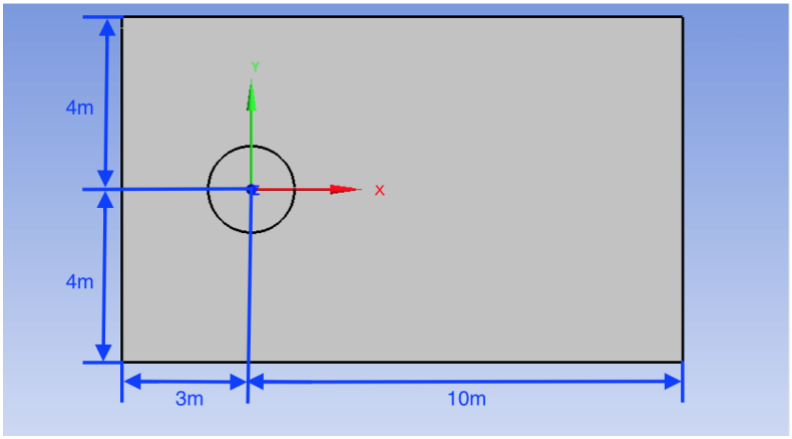

Figure 5. Cylinder model in computational domain

Additional geometries were created for actuator cylinders with diameters of 0.5m, 1m, and 4m. For these additional cases, the computational domain remained the same; however, each case was scaled proportionally considering the new diameter of the cylinder. This ensured that the far field pressure condition that $p \to p_\infty$ as $x \wedge y \to \infty$ was not violated.

A hybrid grid with quadrilateral and triangular cells featuring inflation about the periphery of the actuator cylinder is used in all cases. To establish grid independence, nine mesh refinement studies were performed. For each case the maximum and minimum element sizes were specified and three levels of smoothing were used to control skewness. The inflation was

applied to both the inside and outside faces of the actuator cylinder. For inflation sizing, the first layer height, maximum number of layers, and growth rate were specified. The total number of elements in each mesh is shown in Table 1. The interval angle used to calculate C_p decreased as the number of elements was increased.

Table 1. Series of mesh refinements with number of elements

Mesh	1	2	3	4	5	6	7	8	9
Elements	1,165	2,633	8,495	30,525	113,877	161,285	228,534	440,906	752,306
$\Delta\boldsymbol{\theta}$ (Degrees)	18.00	13.85	6.92	3.43	1.72	1.43	1.20	0.86	0.69

For each refinement, the power coefficient was calculated. The results are shown in Fig. 7.

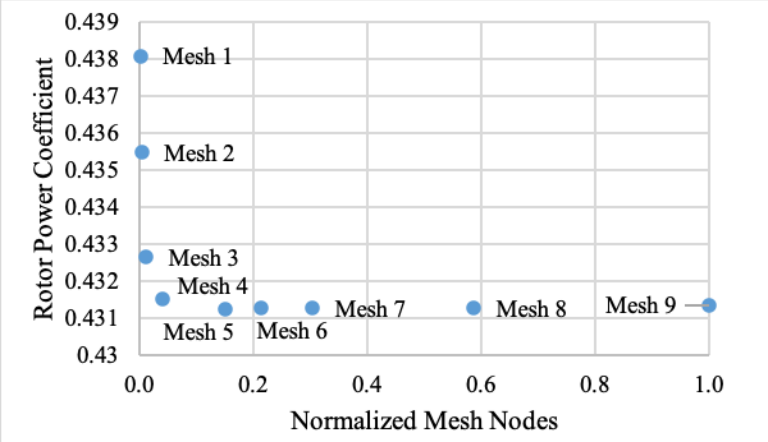

Figure 6. Mesh independence study

It can be noted that the coarser meshes result in higher values of C_p. Considering Eq. 6, this was expected since the coarser a mesh is, the larger is the value of $\Delta\theta$ and consequently the lower is the number of points involved in the Riemann sum. For meshes # 5-9, minimal change in C_p can be observed. Therefore Mesh # 5 was chosen to minimize computational requirements. For this

mesh, shown below, the converged solution had a percentage difference of only 0.26% from the solution on Mesh # 9 and required significantly less computational time.

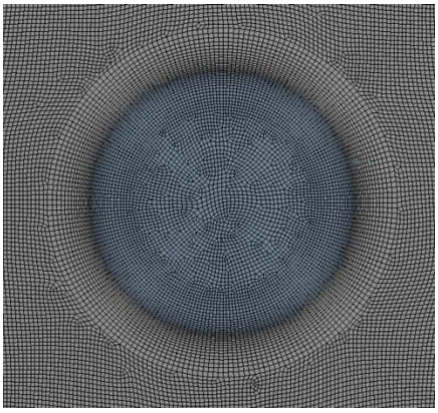

Figure 7. Hybrid mesh #5 in computational domain

2.2 Numerical Model

In Madsen's formulation of the Actuator Cylinder, Euler equations are solved. This indicates that the flow is inviscid. In this study, the incompressible RANS equations are solved to model the turbulent viscous flow. By including shear forces, the flow is no longer laminar and a turbulence model is required. Due to its proven success with external aerodynamic flows, the Spalart-Allmaras (SA) turbulence model was employed.

The transport variable for the SA model is denoted as $\tilde{v}$. This variable is equivalent to the turbulent kinematic viscosity. The transport equation has the form:

$$\frac{\partial}{\partial t}(\rho\tilde{v}) + \frac{\partial}{\partial x_i}(\rho\tilde{v}u_i) = G_v + \frac{1}{\sigma_{\tilde{v}}}\left[\frac{\partial}{\partial x_i}\left\{(\mu + \rho\tilde{v})\frac{\partial\tilde{v}}{\partial x_j}\right\} + C_{b2}\rho\left(\frac{\partial\tilde{v}}{\partial x_j}\right)^2\right] - Y_v + S_{\tilde{v}} \qquad (8)$$

where G_v is the generation term for the turbulent viscosity and Y_v is the destruction term for the turbulent viscosity in near wall regions. $S_{\tilde{v}}$ is an arbitrary source term. $\sigma_{\tilde{v}}$ and C_{b2} are constants [12]. By solving only one transport equation, the solution process is less computationally intensive.

For the boundary conditions, the left side of the computational domain is considered as a velocity inlet. Velocities are only in the *x* direction and range from 1m/s to 24m/s. The right side of the domain is considered as a pressure outlet. Both the top and bottom exterior edges of the computational domain are modeled as far field velocity conditions with the same velocity as of the inlet. Since the entire domain was modeled as a fluid medium, the actuator cylinder zone type was double-sided. To model the pressure jump for a double-sided zone, a fan boundary condition is set around the periphery of the cylinder. In order to properly orient the fan boundary condition toward the far field outlet, the direction of the fan was reversed. A 360-point profile is created using Eq. 4 for the pressure jump of the fan.

To determine the optimal numerical algorithm for the model, initial tests were performed using SIMPLE, SIMPLEC, and the Coupled algorithm in ANSYS Fluent. Trials were performed for C_D = 0.5, D = 4, and V_∞ = 1m/s and the output power was calculated. The difference in calculated power for each algorithm was found to be just over a tenth of a percent. SIMPLE and SIMPLEC are both segregated algorithms. This means that they solve conservation of momentum and the pressure-based continuity equations used in this model separately. The Coupled algorithm solves the equations simultaneously [13]. For this reason, the Coupled algorithm was selected; convergence was achieved in a fraction of the iterations as compared to SIMPLE and SIMPLEC. For convergence, a criterion of 10^{-5} is used for the continuity equation, the momentum equations, and for the turbulent kinetic viscosity associated with the Spalart-Allmaras model.

Chapter 3: Results and Discussion for a Single VAWT

3.1 Comparisons of Computed Results with Inviscid Theory

For C_D = 0.5, three primary flow field characteristics are compared:

1. The *x*-component of the velocity along the centerline
2. The centerline pressure
3. The wake velocity profiles at three designated positions

As can be seen in Fig. 8 (a) and (b) below, there is good agreement with the inviscid theory for *x*-velocity component and for the pressure distribution on the centerline.

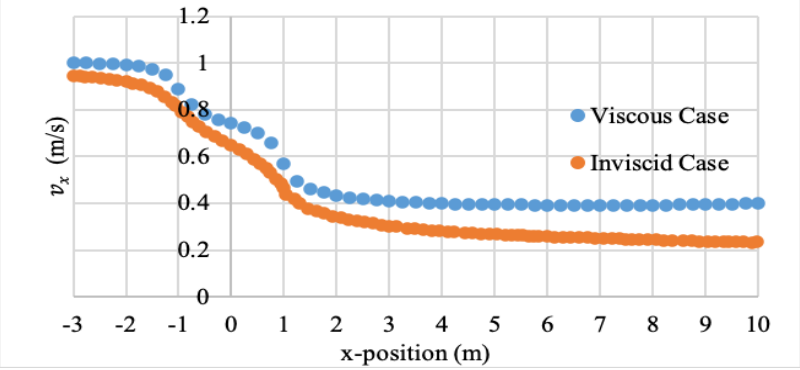

Figure 8 (a). v_x vs. x-position for C_D=0.5

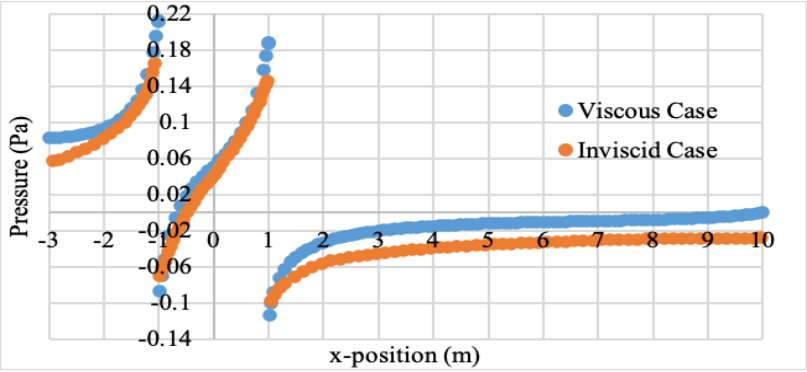

Figure 8 (b). Pressure vs. x-position for C_D=0.5

For the inviscid case, the *x*-component of velocity on the centerline was always less than the velocity magnitude upstream to the cylinder. This resulted in a slightly downshifted profile. There was also a greater reduction in wake velocity for the inviscid case. For the viscous case, the wake velocity began leveling out as *x* approached 10m. The only other observed difference was that the viscous case had a more pronounced change in v_x between the leading and trailing edge of the cylinder. This occurs between the *x*-coordinates (-1, 1).

In comparing the *x*-component of velocity at different positions in the wake, the inviscid case was found to have a slightly wider wake profile and a greater reduction in velocity than the viscous case with $m = 1$. This is shown in Fig. 9 where the inviscid wake width is normalized relative to the actuator cylinder diameter of 2m.

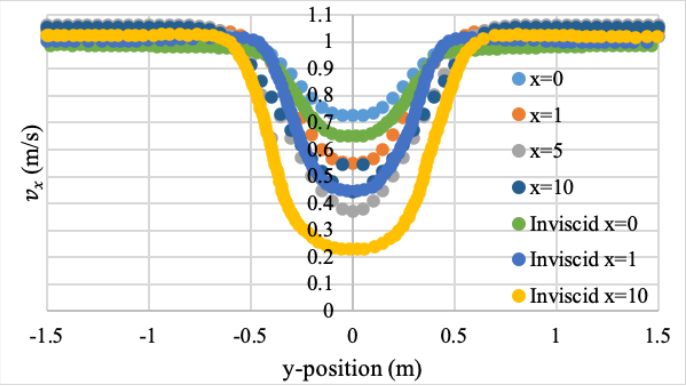

Figure 9. Comparison of inviscid and viscous wake profiles for *m*=1

As previously mentioned, higher values of the exponent *m* result in a wider and more uniform wake profile. For the more uniform profile, the wake velocity acts similar to a weighted average; the wake spans a wider region and the percent reduction in velocity is of a lower magnitude located between the initial maximum and minimum. This is shown below for a comparison of $m = 1$ and $m = 5$.

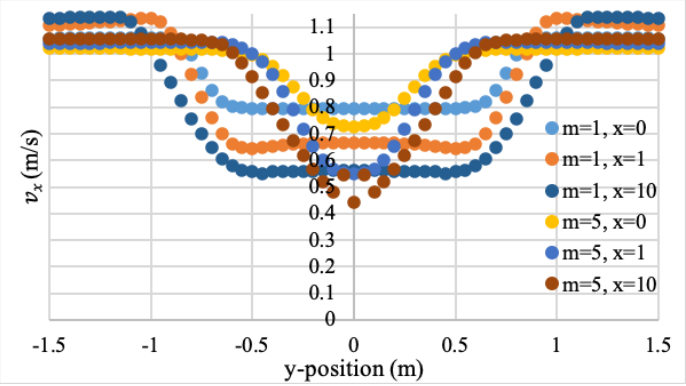

Figure 10. Comparison of wake profiles for m = 1 and m = 5

This effect can be attributed to the pressure profile. As m increases, the pressure gradient as a function of angle becomes increasingly uniform at the leading and trailing edges. This can be seen below at angles of 90° and 270°.

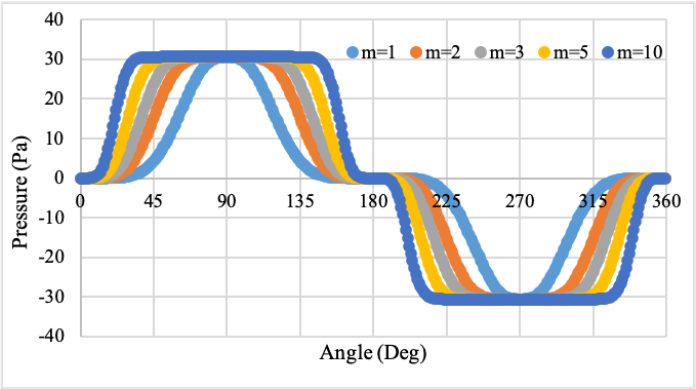

Figure 11. Comparison of inviscid and viscous wake profiles for m=10

For the inviscid case, a 77% reduction in freestream velocity was observed at x = 10m. Comparatively, a maximum reduction of 60.3% was observed for the viscous case with m = 1. The point that the minimum velocity occurred was also further upstream near x = 5m for the viscous case. After this point the velocity began to slowly rebound. This is shown in Fig. 12.

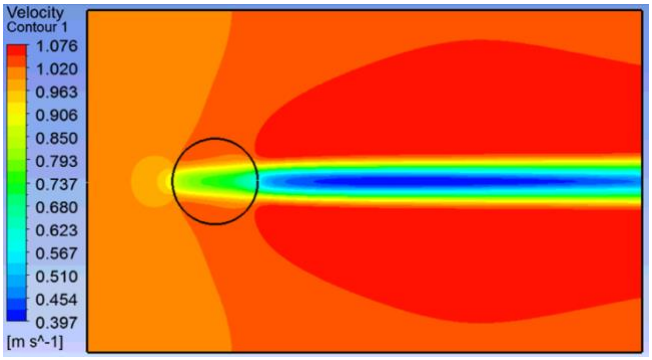

Figure 12. Velocity contours for V_∞ = 1m/s, m = 1

By expanding the domain and placing the actuator cylinder further downstream, there was less difference between the velocity reduction for the inviscid and viscous cases.

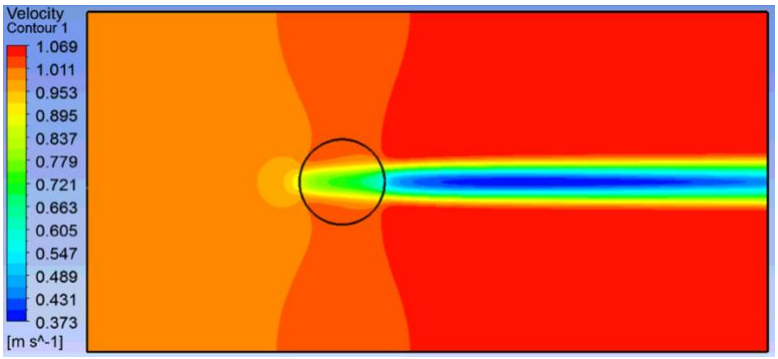

Figure 13. Velocity contours for V_∞ = 1m/s, m = 1 with expanded domain at leading edge

Here, the distance from the leading edge of the domain to the center of the actuator cylinder was increased from 3m to 6m. This resulted in a 6.43% lower minimum velocity in the wake. As seen below, increasing the domain further produced negligible change.

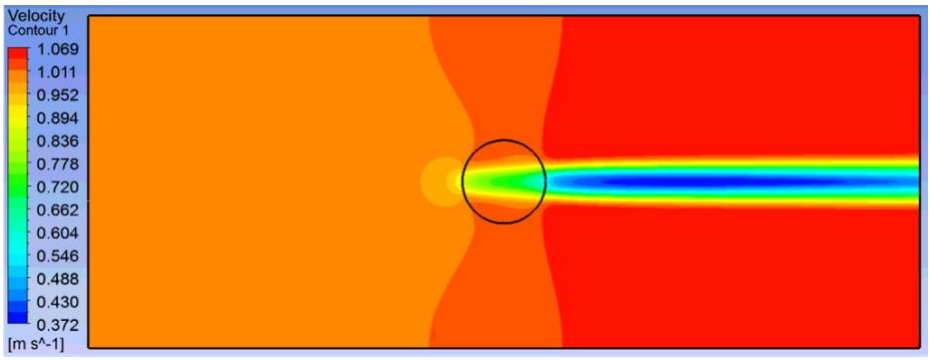

Figure 14. Velocity contours for V_∞ = 1m/s, m = 1 with expanded domain on both sides

By increasing the freestream velocity, the normalized minimum velocity in the wake also decreased. For V_∞ = 10m/s, the normalized minimum velocity in the wake was 0.366m/s. This is 8.47% lower than the minimum wake velocity found for V_∞ = 1m/s with the same domain. This trend continues for higher values of V_∞. For V_∞ = 24m/s, the normalized minimum velocity relative to the freestream velocity was 0.362m/s, which is 9.67% lower than the minimum for V_∞ = 1m/s.

For C_D = 0.54, additional comparisons were made for v_x and velocity angle around the cylinder's periphery. As shown in Fig. 15 (a) and (b), the inviscid case has more gradual changes in both velocity angle and velocity reductions at the leading and trailing edges.

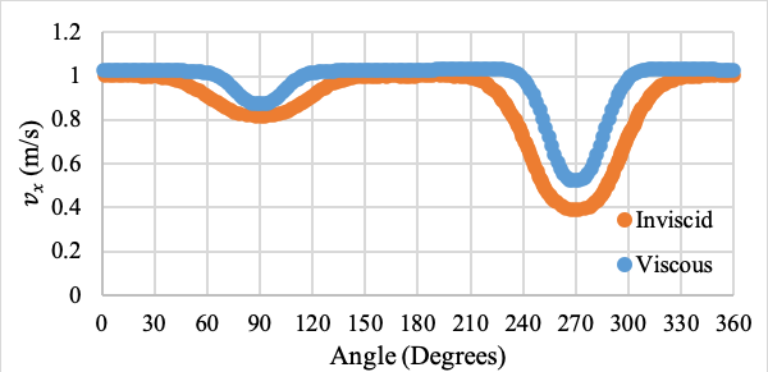

Figure 15 (a). Comparison of v_x around the periphery of actuator cylinder

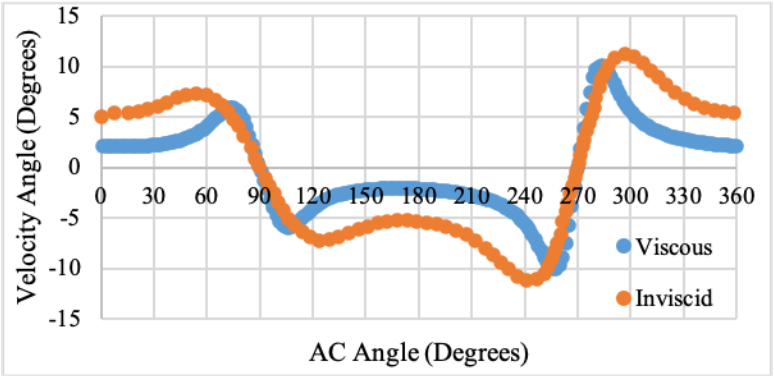

Figure 15 (b). Comparison of velocity angle around the periphery of actuator cylinder

Vorticity was also compared for C_D = 0.54.

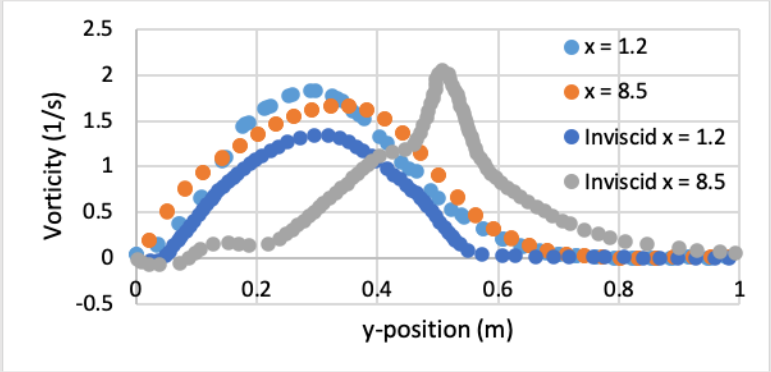

Figure 16. Comparison of vorticity at two downfield locations

For each model, the pressure gradient across the actuator cylinder created vorticity in the fluid [14]. Similar behavior was seen at x = 1.2m for the viscous and inviscid cases; however, the magnitude of the vorticity was nearly 37% higher for the viscous case. Further downstream at x = 8.5m, the vorticity for the viscous case exhibited slight reduction while an abnormal peak was observed for the inviscid case. As outlined by Madsen, this behavior was indicative of a tendency toward instability at greater distances in the wake [11]. For the viscous case, a wider profile with a lower magnitude at x = 8.5m relative to x = 1.2m is representative of the diffusion of vorticity for the flowing fluid [14].

3.2 Computation of Flow Fields and Power Generation

For a single actuator cylinder of different diameters, the relationship between the freestream velocity and rotor power is computed. As previously mentioned, this was done for freestream velocities ranging from 1m/s to 24m/s for four different diameters of the actuator cylinder. For each case, the power was calculated as Watts per unit length of the cylinder as given in Fig. 17.

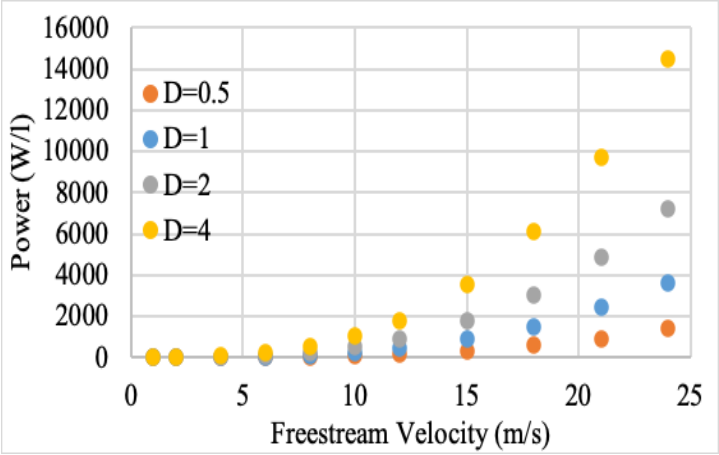

Figure 17. Comparison of velocity angle around the periphery of actuator cylinder

The relationship between the generated power and the freestream velocity is found to be nearly cubic. This result is in line with the theoretical expectation, which can be noticed from the denominator of Eq. 2. In comparing power versus diameter, the relationship was found to be nearly proportional. This result, as can be seen in Fig. 18, was true for the entire range of freestream velocities.

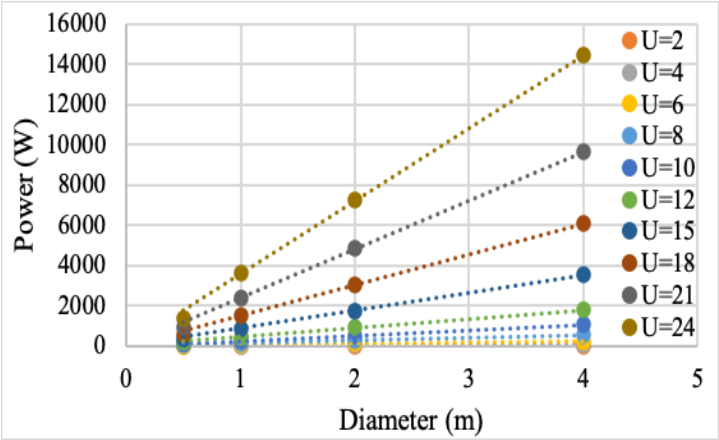

Figure 18. Comparison of velocity angle around the periphery of actuator cylinder

When the diameter was doubled, the power was also found to approximately double. As can be seen in Eq. 6, this is also in line with theory. However, it should be noted that there was a greater deviation from direct proportionality for the case of D = 0.5m.

Similar cases were executed by varying the exponent m. Computations were performed for freestream velocities of 1m/s to 10m/s and the same near cubic variation in generated power with freestream velocity was obtained. As m increased, more power was generated by the VAWTs. This result is consistent with the inviscid study performed by Madsen [11].

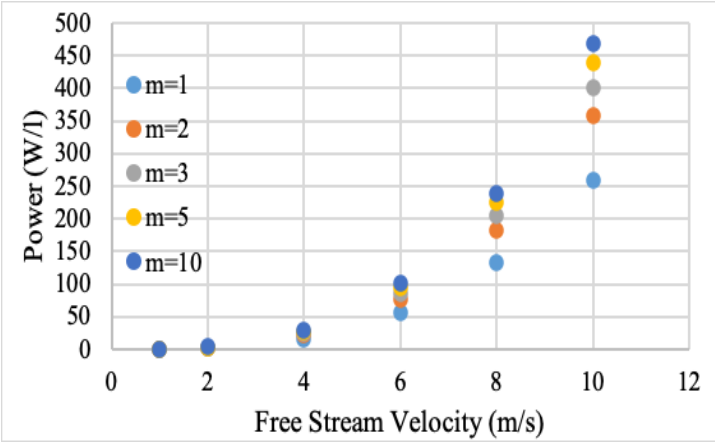

Figure 19. Power generated by the actuator cylinder for various m and freestream velocities

Using the calculated rotor power given in Fig. 20 above, the power coefficients were calculated for various m for a rotor with $D = 1.0$ m and $V_\infty = 10$ m/s.

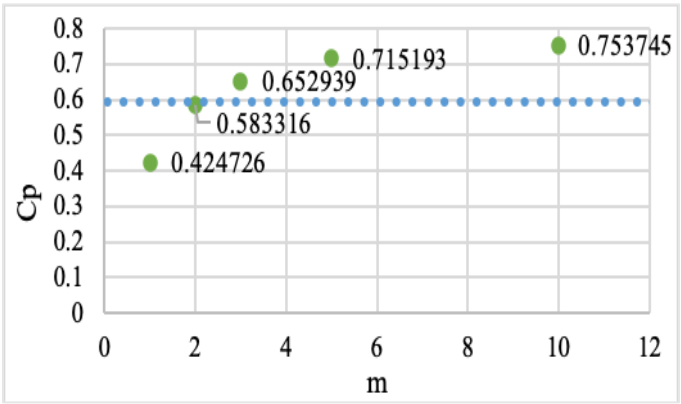

Figure 20. Variation in C_p with m for $D = 1.0$ m and $V_\infty = 10$ m/s

As shown by Madsen [11], for high values of m the power coefficient of the VAWT model exceeds the theoretical Betz limit for HAWTs. This suggests that the Betz limit may not be applicable for VAWTs. In this study, the Betz limit was exceeded at an m = 3 for C_D = 0.5. This

result was found to be independent of turbine diameter and wind speed. Additionally, for m = 1, C_p was found to be approximately 13.6% higher than that in the inviscid study.

A uniform load form was used for formulation of the Betz limit for an ideal HAWT [11]. For this reason, it was necessary to determine a suitable value for m such that a uniform load form was present in the determination of an ideal VAWT. To achieve this, m was taken to increase with a constant freestream velocity of 10m/s for D = 2. The power was calculated for each case until the effects of increasing m became negligible.

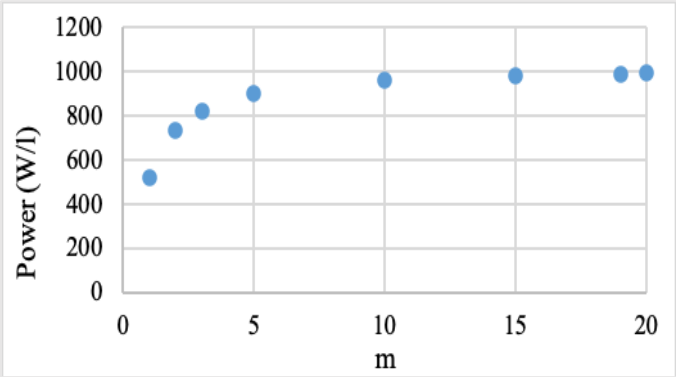

Figure 21. Determination of m for ideal VAWT

The percent difference between consecutive values of m associated with Fig. 21 are given below in Table 2.

Table 2. Percent difference in output power as a function of m

m	1	2	3	5	10	15	19	20
Power (W)	523	732	821	904	963	983	990	991
% **Difference**	-	28.5	10.9	8.88	6.48	2.00	0.767	0.136

Note. The column referencing the percent difference indicates the difference between that column and the left value of m immediately before

For low values of m, any increase in m resulted in dramatic differences in power. As m increased, the change in power became less pronounced. After observing minor changes between m = 15 and m = 20, an additional refinement case for m = 19 was implemented. From these trials, m = 20

was determined to be the appropriate choice for an ideal VAWT using Actuator Cylinder Theory.

The velocity contours for selected values of *m* are shown below. For each case the model parameters were $V_\infty = 10$ m/s, C_D = 0.5, and D = 2m.

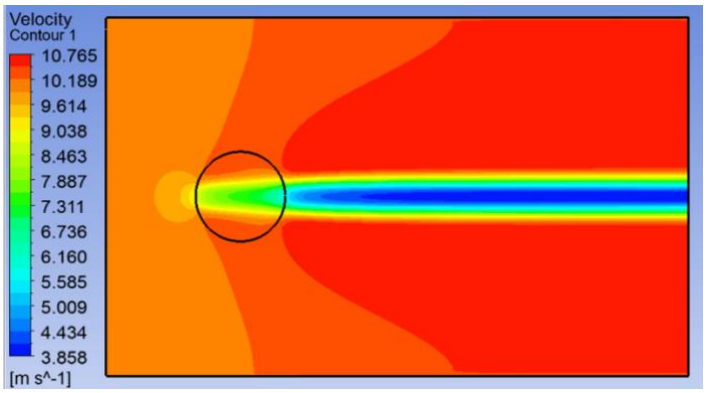

Figure 22 (a). Velocity contours for *m* = 1

For the actuator cylinder with *m* = 1, the wake width was only 50% of the total diameter. This is an effect of the pressure profile. As can be seen in Fig 22 (b), for low *m* the pressure jump has narrow peaks at 90° and 270°.

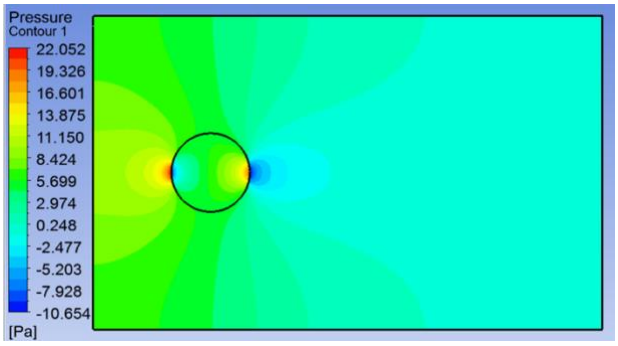

Figure 22 (b). Pressure contours for *m* = 1

As *m* increased, the width of the wake grew proportionally to the region with a pressure jump magnitude near Δp_{max}. For *m* = 3 and *m* = 5, the wake width made up approximately 75% and 85% of the total diameter of the actuator cylinder. As the wake width increased, the induced

velocity outside of the wake and the minimum velocity in the wake also increased. This can be seen below in Figs. 23-25.

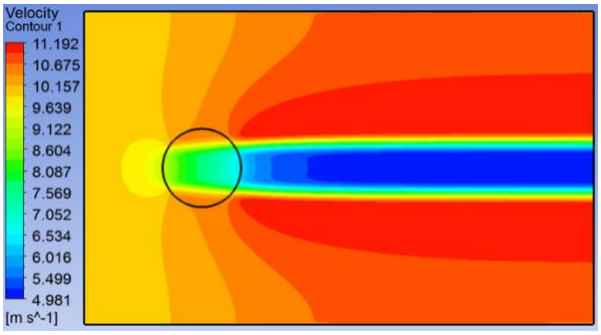

Figure 23 (a). Velocity contours for m = 3

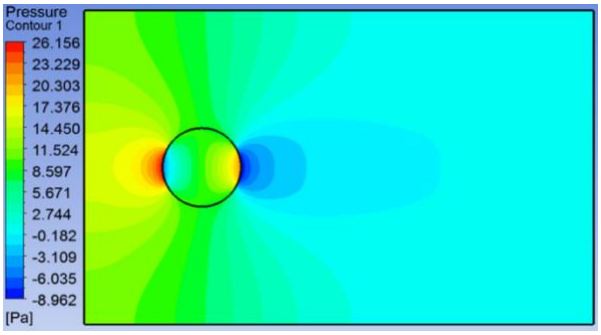

Figure 23 (b). Pressure contours for m = 3

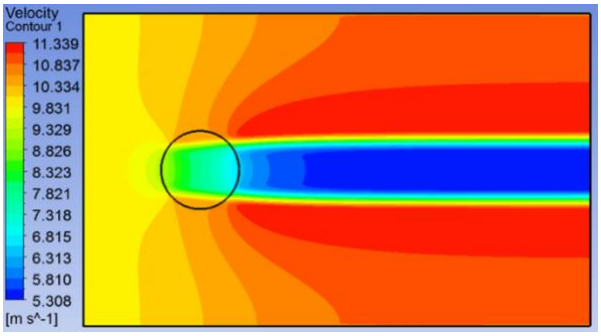

Figure 24 (a). Velocity contours for m = 5

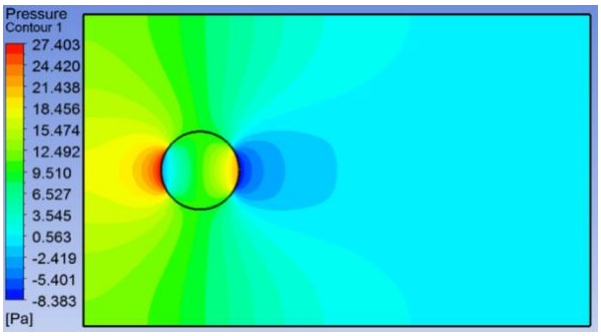

Figure 24 (b). Pressure contours for m = 5

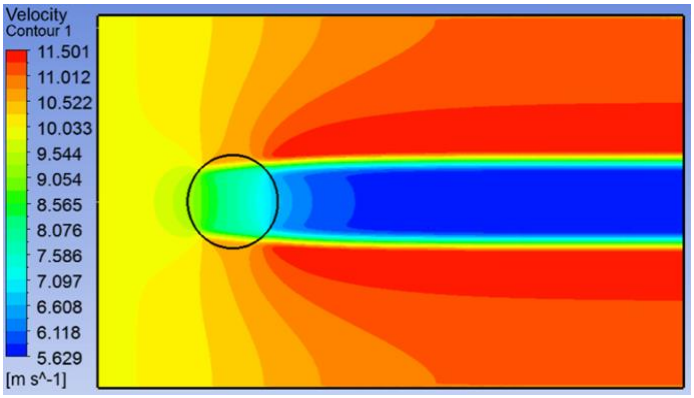

Figure 25 (a). Velocity contours for m = 10

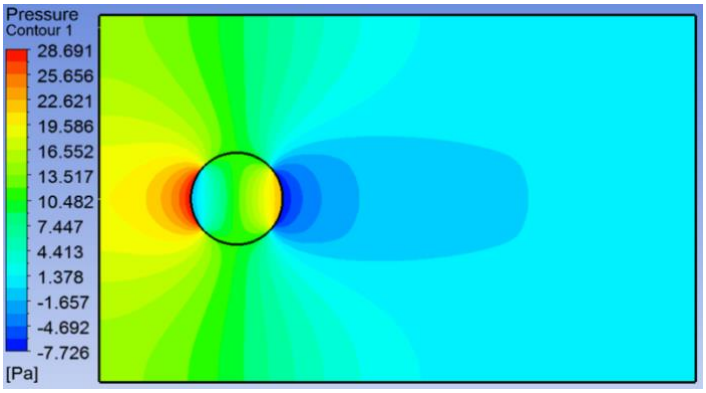

Figure 25 (b). Pressure contours for m = 10

For the ideal case, the regions of the pressure jump with magnitude near zero were more limited to points near 0° and 180°. This resulted in a wake width that was 3% wider than the diameter of the actuator cylinder as shown in Fig. 26.

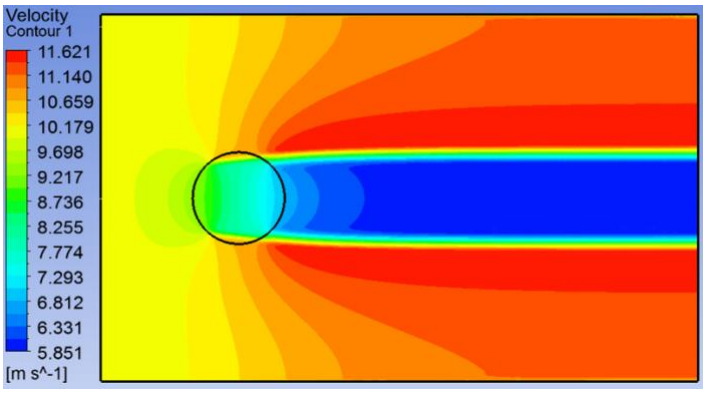

Figure 26 (a). Velocity contours for m = 20

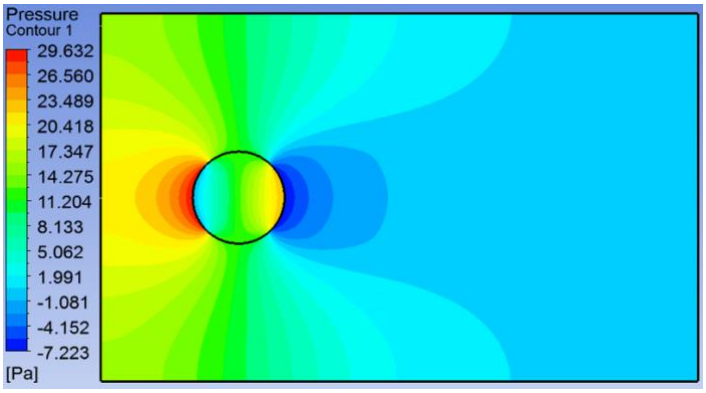

Figure 26 (b). Pressure contours for m = 20

3.3 Conclusions

Based on the single actuator cylinder study, the following conclusions can be drawn:

(1) This is the first time in the literature that an actuator cylinder model for a VAWT has been studied using the RANS equations with a turbulence model. This allows for quick but reasonably accurate evaluation of power generation from VAWTs of different diameters at various wind speeds. The turbulent flow model captures the wake behind the VAWT fairly accurately which is important in determining the optimal layout of VAWTs in wind farms. The use of CFD is enormously expensive for such evaluations.

(2) The viscous flow computations of downstream velocity and pressure have good agreement with the inviscid Euler corrections in terms of trends and magnitudes; the differences are due to

the viscous effects accounted in the present model. The viscous wake behavior, although slightly different as expected is generally consistent with the theoretical inviscid model.

(3) The computed power coefficient in this study is consistently 13% higher than the inviscid case. It can be attributed to the fact that wake is more accurately modeled in the present study while it is approximated by invoking unrealistic assumptions in the inviscid model.

(4) For the formulation of an ideal VAWT, a pressure jump exponent of $m = 20$ is appropriate.

(5) While the Betz limit has been demonstrated to be applicable for HAWTs, this study suggests that it is not applicable to ideal VAWTs. This result was also found in the original inviscid study by Madsen.

Chapter 4: Multiple Wake Interactions in VAWT Arrays

4.1 Physical Model and Grid for VAWT Arrays

Previous studies have indicated that VAWTs may require less space among turbines than traditional HAWTs in a wind farm [15]. Additionally, an increase in efficiency has been demonstrated for properly spaced pairs of VAWTs compared to isolated VAWTs. In this study, two and three VAWT arrays have been created. For both cases, an actuator cylinder diameter of 2m was used with $V_\infty = 10$ m/s.

For the two turbine cases, the actuator cylinders were directly in line with each other with the lower turbine centered about the origin. This is important because the definition of the radial velocity in Eq. 6 for the power calculation is dependent on the position relative to the coordinate axes. As such, all of the power calculations were made for the lower turbine.

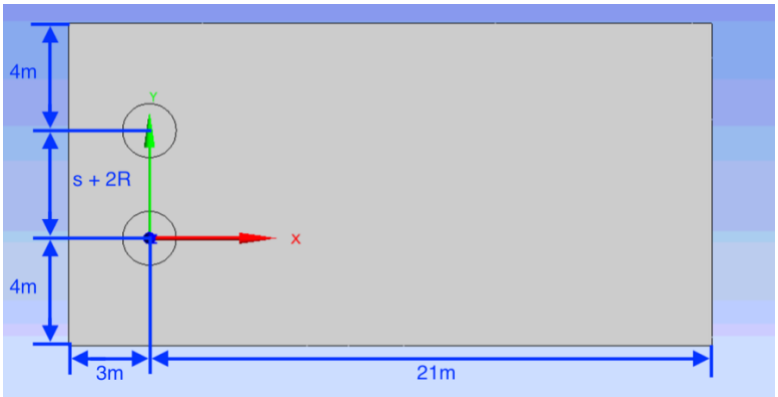

Figure 27. Geometry for two turbine configuration

To calculate the power of the upper turbine, an additional geometry with the upper turbine centered about the origin would have been required. However, due to symmetry this was

omitted; the difference in power between the two turbines remains negligible so long as they are directly in line with each other.

To determine the ideal spacing, geometries were created for s = 0.5m, s = 1m, s = 2m, and s = 4m. Additionally, to verify that the power of each turbine approached the power of an isolated VAWT as spacing became large, three additional cases with s = 8m, s = 16m, and s = 24m were created. For each spacing, the same increments of m from the single turbine cases were applied with the addition of m = 20 for the ideal case. As seen in Fig. 27, the remaining distances in the domain were constant. The distances between the front edge to the center of the actuator cylinders was 3m and the distances between the top and bottom edges to the center of the nearest actuator cylinder were 4m each. Twenty-one meters was used for the distance between the centers of the cylinders to the far field boundary. Here, a larger distance was chosen relative to the single actuator cylinder case in order to allow for the eventual addition of a third VAWT downfield. By including a greater percentage of the wake, the error in the solution is also reduced.

For three VAWT arrays, an additional turbine was added directly between the leading row at a variable distance x_{DF} downstream. The remaining distances in the geometry were the same. For the four primary VAWT spacings addressed above, the downfield distance was chosen to vary by increments of 0.5m ranging from an even alignment to 3.5m downstream. Here, the spacing is measured from the trailing edge of the front VAWTs to the leading edge of the downfield actuator cylinder. This is demonstrated below for a spacing of 2m and a downfield distance of 3.5m.

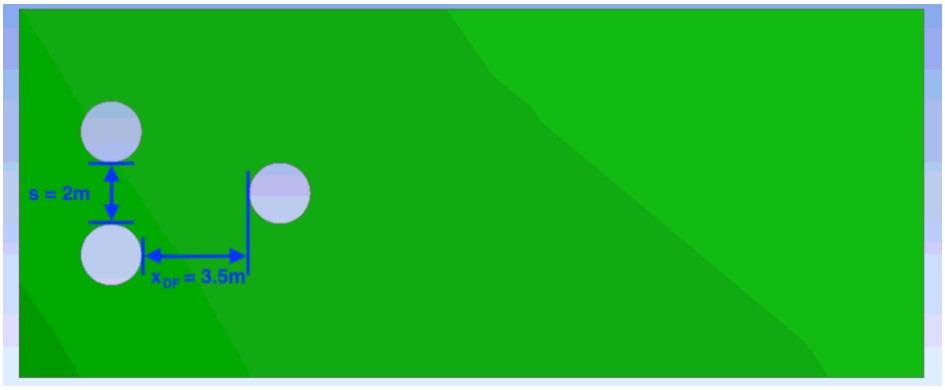

Figure 28. Three turbine geometry with s = 2m and x_{DF} = 3.5m

For both the two and three VAWT cases, the same mesh #5 from the mesh independence study was used. This is shown below in Fig. 29 for two and three actuator cylinders, each with s = 1m. For the three turbine case shown below, the downfield distance was 1m

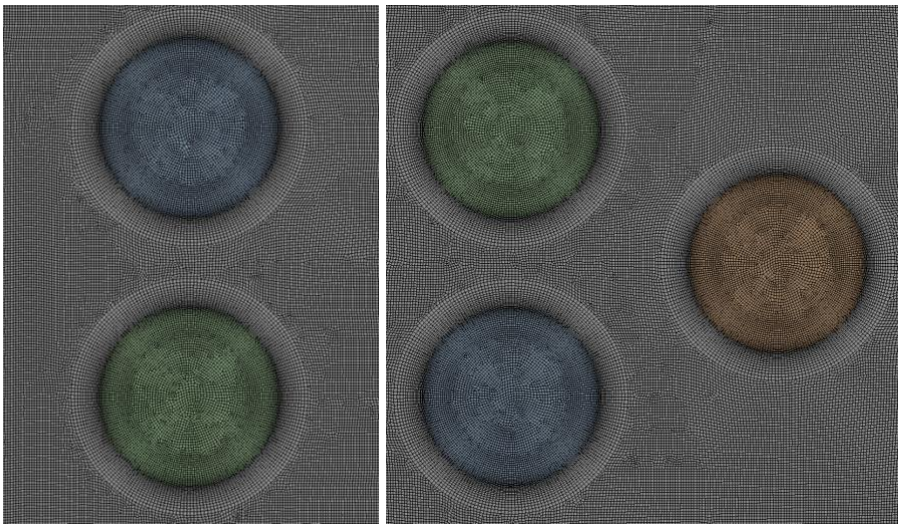

Figure 29. Hybrid mesh #5 for two and three turbines with s = 1m.

4.2 Numerical Model for VAWT Arrays

For the analysis of multiple wake interactions, the Incompressible RANS equations were solved using the SA model for turbulence with identical boundary conditions as before. For the pressure profile of the reversed fan boundary condition, the two turbine cases had 720 points and the three turbine cases had 1080 points. As seen in Eq. 5, the coefficient for the pressure jump is

dependent on the freestream velocity. For two turbine cases, the freestream velocity could be taken directly as the velocity inlet boundary condition. However, for three VAWT arrays the velocity for the downfield pressure jump was the resulting induced velocity from the leading row of turbines. This included regions of increased velocity, as well as the wake regions if there was any overlap between the *y*-position of the downfield actuator cylinder and the leading row. This is demonstrated in Fig. 31 below for a spacing of 0.5m. The downfield actuator cylinder is outlined; however, no pressure jump is applied for this case.

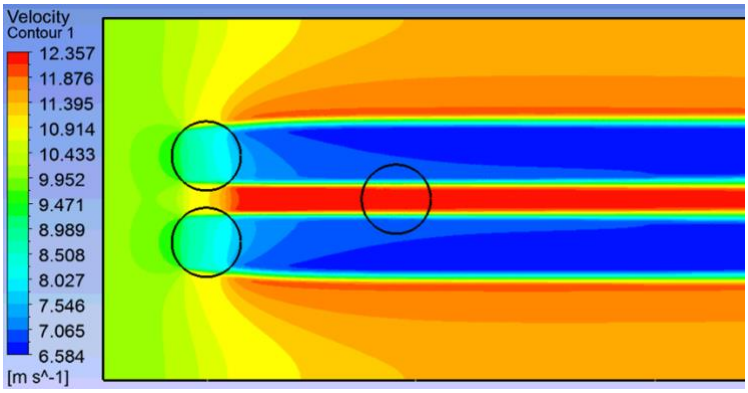

Figure 30. Pressure jump calculation for the downfield actuator cylinder

A probe was used at the location of the leading edge of the downfield actuator cylinders to capture the velocity profile. This was performed for every tenth a meter on the *y*-interval (-1, 1).

For the numerical algorithm, the Coupled algorithm was initially implemented. While the Coupled algorithm was successful with a single actuator cylinder, the algorithm failed to converge for cases with two and three actuator cylinders. For multiple fan boundary conditions, the SimpleC algorithm always lead to a converged solution using the same convergence criteria of 10^{-5} and was thus implemented.

4.3 VAWT Array Results and Discussion

4.3.1 Comparisons of Two VAWT Geometries

Power was calculated for each combination of VAWT spacing and *m*. The trend in rotor power as spacing increased was plotted relative to the power of a single actuator cylinder for the same value of *m*. For *m* = 1, the following trend was found. The power for the isolated actuator cylinder is represented by the orange dotted line.

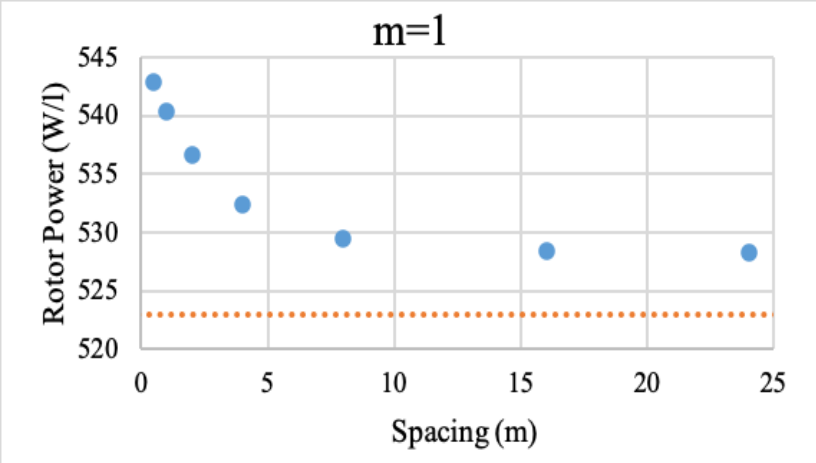

Figure 31. Power vs. *s* for *m* = 1

As can be seen above in Fig. 31, as spacing increased the power of each actuator cylinder in the pair approached the power from the isolated case. This is a required result for the model. While the behavior appears to be asymptotic at a value greater than the isolated case, the percent difference is very small. At *s* = 24m, the output from a VAWT in the pair is only 1.01% higher than the output of an isolated VAWT.

The same asymptotic trend was found for the remaining values of *m*. For each case, the percent difference between an isolated VAWT and a VAWT included in a pair never exceeded 1.01%. However, for the remaining cases, the power approached an asymptote slightly below the

power of a single actuator cylinder rather than above. This is shown in Fig. 32 for the ideal case $m = 20$.

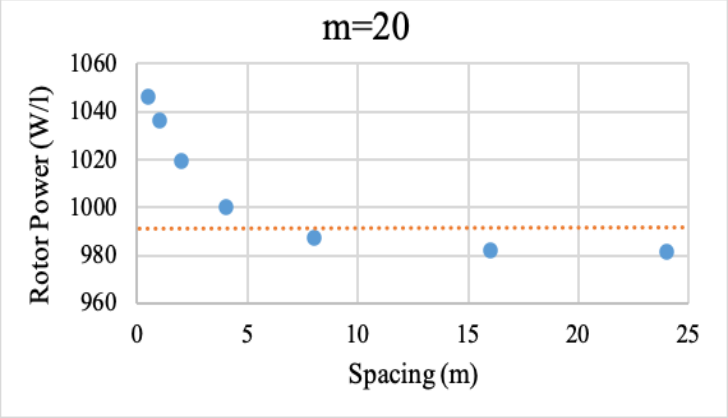

Figure 32. Power vs. s for $m = 20$

For each value of m, it can be observed that the power output increased as $s \rightarrow 0$m. This result was due to interacting regions of increased velocity outside of the actuator cylinders' wakes. To see this trend, consider the velocity contours below in Fig. 33.

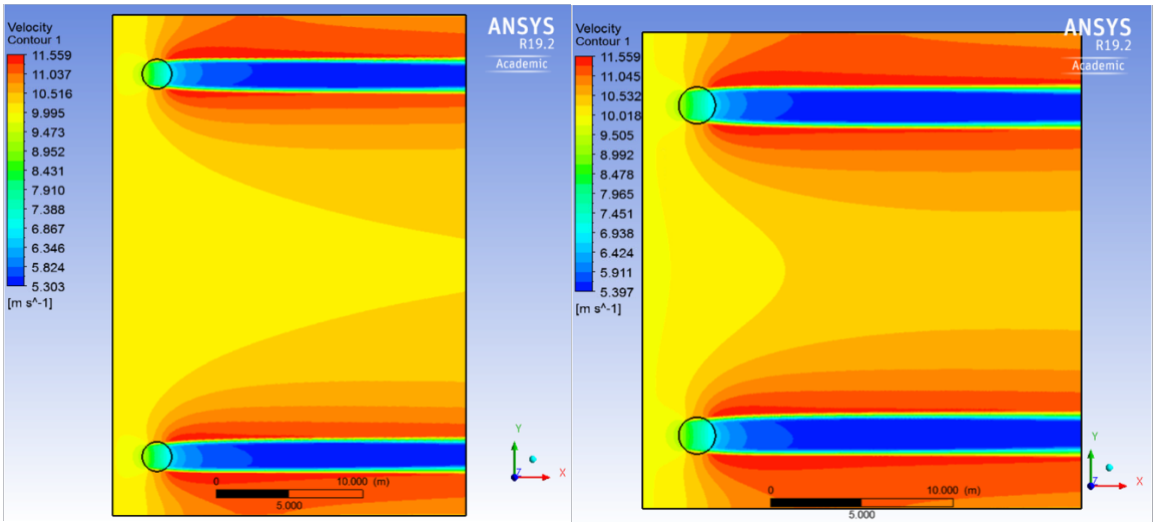

Figure 33. Velocity contours of two turbines with s = 24m and s = 16m

For s = 24m, there is a gap between the wake profiles where the freestream velocity remains unaffected. As spacing decreases, the wakes become close enough to interact. This is shown on the right for s = 16m, as well as in Fig. 34 below for s = 8m.

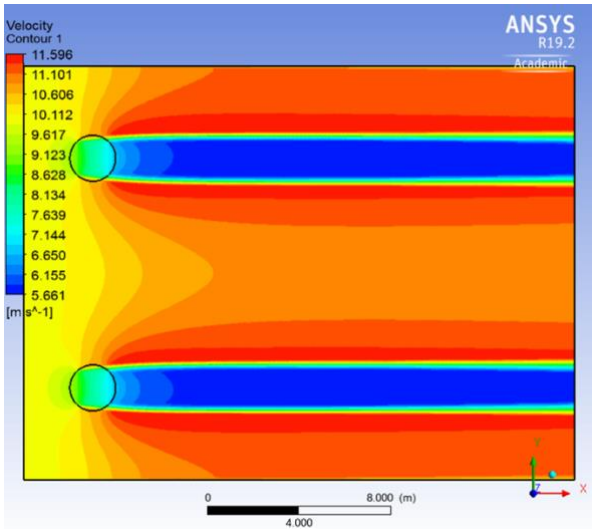

Figure 34. Velocity contours of two turbines with *s* = 8m

As the spacing decreases, greater wake interaction results in an increase in magnitude for the induced velocity outside of the wake as shown in Fig. 35.

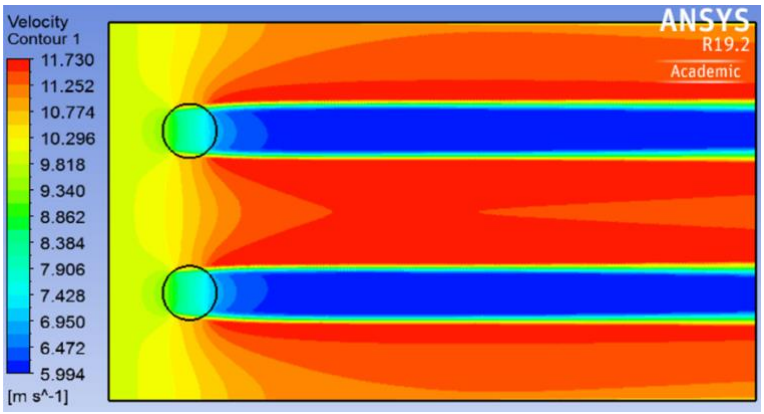

Figure 35. Velocity contours of two turbines with *s* = 4m

Here, the maximum velocity outside of the wake is 11.730m/s. For the single actuator cylinder in Fig 26 (a), the maximum velocity was 11.623m/s. This effect, which demonstrates the benefits of properly aligned VAWTs, becomes more pronounced as spacing decreases as shown in Fig. 36.

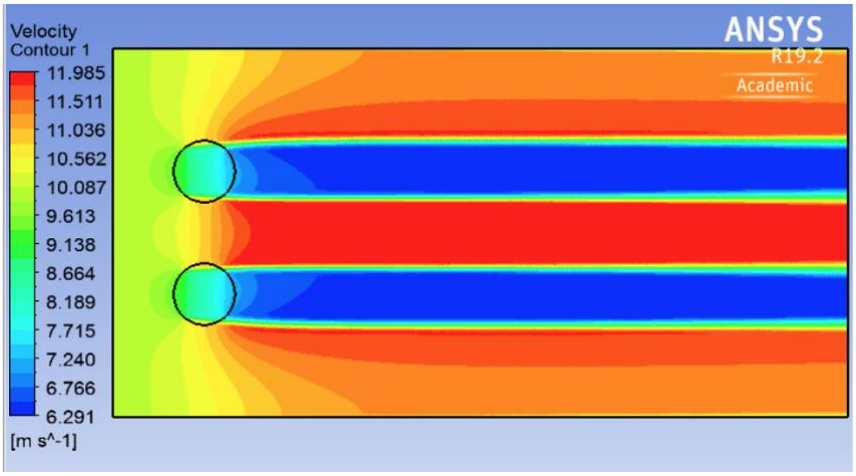

Figure 36 (a). Velocity contours of two turbines with *s* = 2m

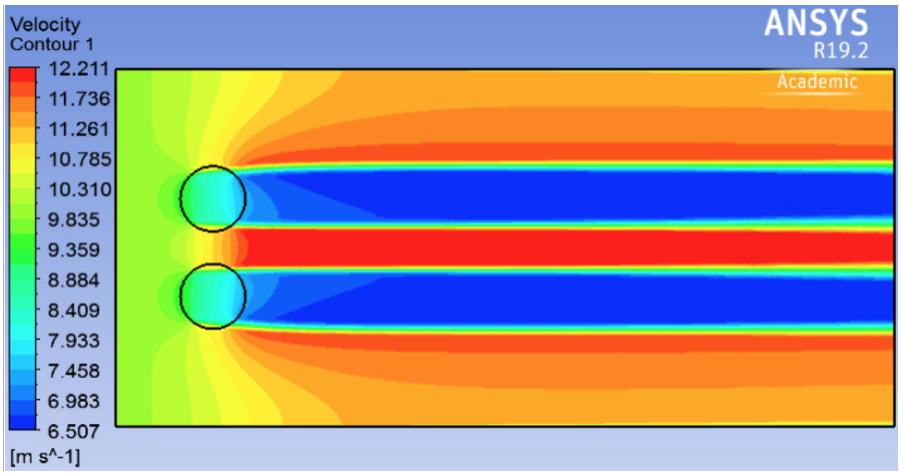

Figure 36 (b). Velocity contours of two turbines with *s* = 1m

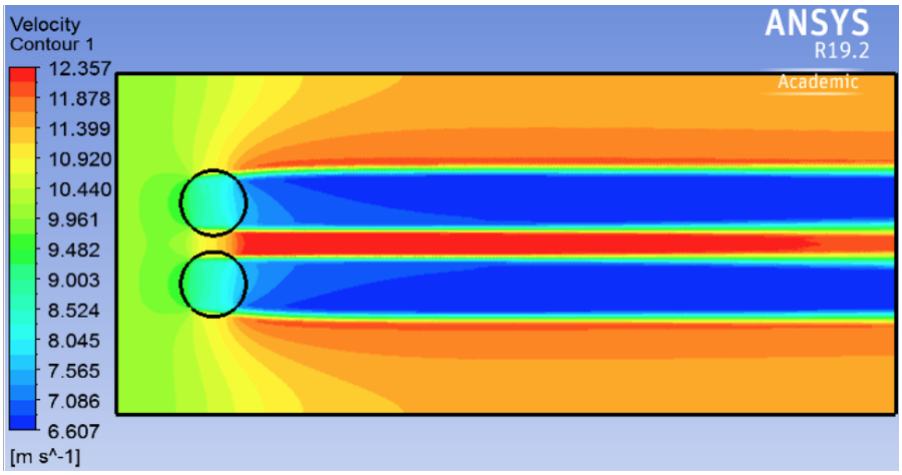

Figure 36 (c). Velocity contours of two turbines with *s* = 0.5m

While the trend of increasing power with decreasing spacing exists across all values of *m*, the effects are non-uniform. As previously observed in Fig. 22 (a) through Fig. 26 (a), the wake width changes proportionally with *m*. Furthermore, the level of interaction between regions outside of the wakes depends on the spacing. For lower values of *m*, a narrower wake means that the spacing between actuator cylinders is effectively greater. As such, while there is still an increase in performance for VAWTs in a pair as compared to isolated VAWTs, the percent increase is of a lesser magnitude. This is shown below in Table 3.

Table 3. Percent increase in power for VAWT in a pair relative to an isolated VAWT

Spacing	*m* = 1	*m* = 2	*m* = 3	*m* = 5	*m* = 10	*m* = 20
0.5m	3.82	3.32	3.81	4.35	6.75	5.55
1m	3.34	2.67	3.07	3.51	4.05	4.51
2m	2.62	1.67	1.91	2.20	2.55	2.84
4m	1.81	0.53	0.61	0.70	0.80	0.90

Note. For higher spacing, the behavior approaches isolated VAWT and asymptotic behavior differs. See Fig. 31 and Fig. 32.

This effect is primarily noticed for small *s* when the ratio of the wake width relative to spacing is at a maximum. For small *m*, the wake width is approximately half of the diameter of the actuator cylinder. This is shown below for *m* = 1.

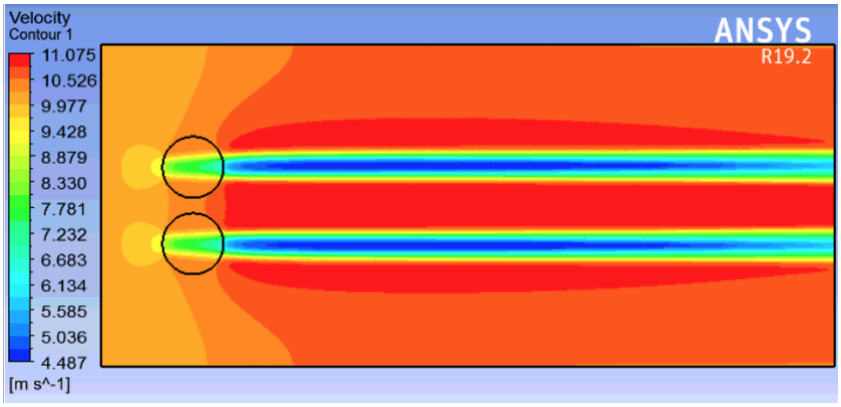

Figure 37. Velocity contours of two turbines with *s* = 0.5m

This means that, while the peripheries of the actuator cylinders are only 0.5m apart, the distance between the wakes is closer to 1m. As such, the interaction between the regions of increased velocity occur at points which are further from the wake; these points have a lower velocity magnitude. For larger *s*, an increase in the wake width becomes less influential because it makes up a smaller percent of the total spacing between cylinders.

To determine if a limit exists for the trend of increasing power with decreasing spacing, a series of case refinements were performed for s = 0.25m, s = 0.1m, and s = 0.01m. Table 4 contains the results for each case using m = 20.

Table 4. Power vs. spacing for ideal actuator cylinder (m = 20)

Spacing	Isolated	0.01m	0.1m	0.25m	0.5m	1m	2m	4m
Power (W/l)	991.4	1052.3	1050.6	1047.1	1046.4	1036.1	1019.6	1000.3
Change in Power	-	6.14%	5.97%	5.62%	5.54%	4.51%	2.84%	0.89%

Note. See Table 3

As can be seen above, no limit was found to exist between decreasing spacing and increasing power for the two Actuator Cylinder Model. The maximum power was for the narrowest spacing of 0.01m. The model thus suggests that an increase in power of approximately 5-6% can be achieved by positioning two turbines together rather than isolating them. Practical limitations should be considered when applying the model. For instance, a spacing of 0.01m is not feasible. Furthermore, the resulting flow field from the actuator cylinder model is symmetric. This means that the effects due to the direction of rotation for each turbine are not present in the model.

4.3.2 Downfield VAWT Optimization

Power calculations for a downfield actuator cylinder were performed for spacing variations of 0.5m, 1m, 2m and 4m using m = 20. As previously addressed, the position of the third actuator cylinder was defined with respect to the trailing edge of the leading row of

VAWTs and ranged from an even alignment to 3.5m downfield. The optimum downfield position was determined for each spacing. Power calculations for the VAWTs in the leading row were repeated in order to gage the complete effect of the downfield VAWT. Total power output for each 3 VAWT array was first compared purely in terms of magnitude and then as a power density by considering the required land area.

For each case, an inverse relationship between power and downfield distance was found for every point beyond x_{DF} = 1m. As can be seen in Fig. 38, the behavior prior to x_{DF} = 1m varied based on the spacing of the leading row.

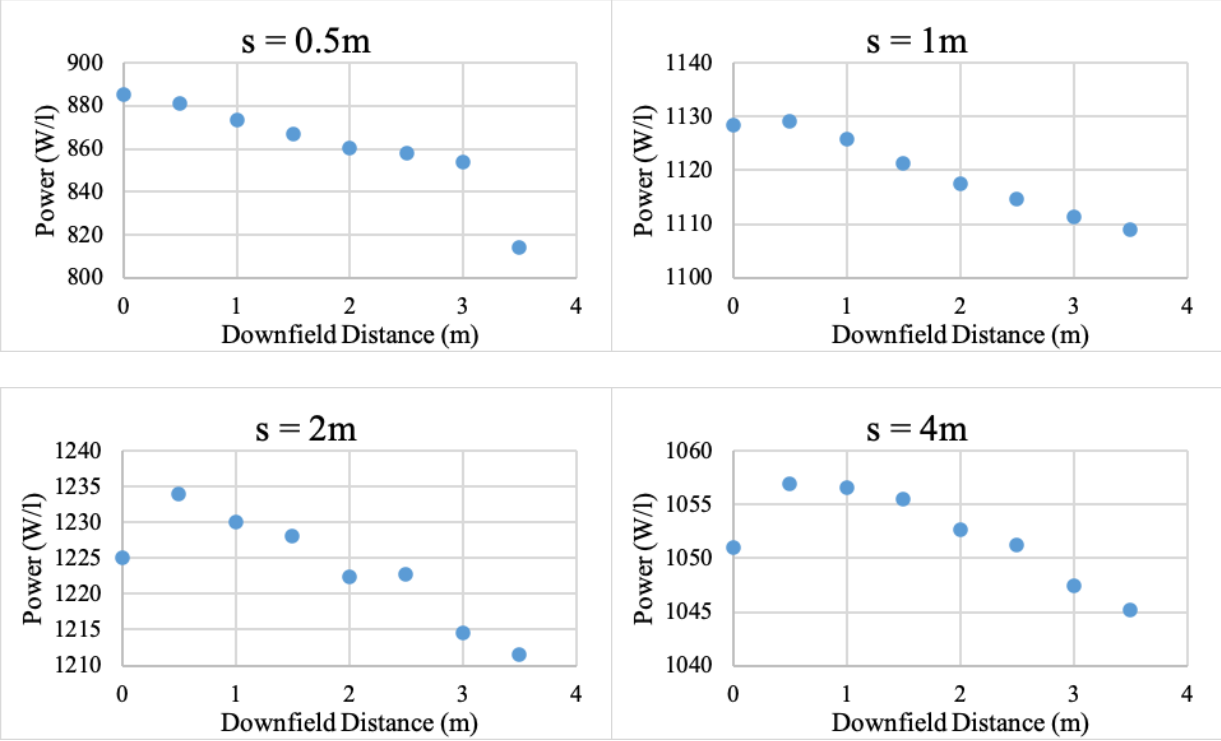

Figure 38. Power vs. x_{DF} for variable spacing

For s = 0.5m, the maximum output was found for the case with an even alignment and decreased at every point thereafter. As spacing increased, the optimum position for the VAWT began to shift slightly downfield. For each of the remaining cases, x_{DF} = 0.5m produced the highest output while the performance for the case with an even alignment decreased considerably.

Narrow spacing was found to have the greatest benefit for two VAWT arrays; however, when a third VAWT was added downfield, a significant reduction in power was observed. This is shown in Fig. 39.

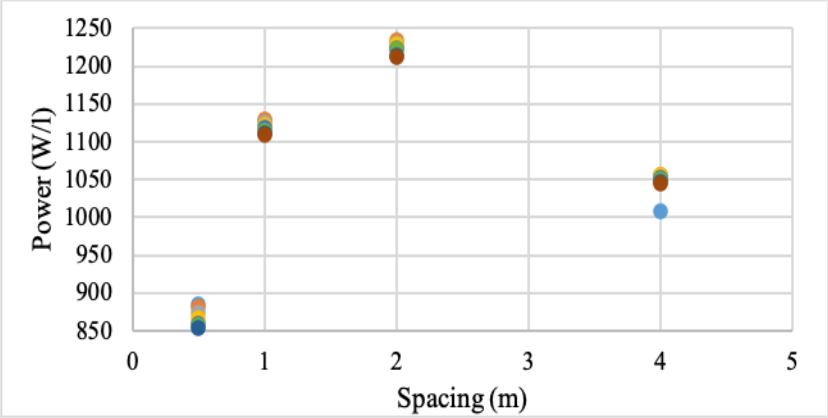

Figure 39. Power comparisons for variable spacing

As can be seen above, the downfield VAWT had the lowest power for s = 0.5m which is not a surprising result. As demonstrated in Fig. 30, the downfield VAWT is exposed to the wake regions of the leading row of VAWTs for cases in which the spacing is less than the diameter of the actuator cylinder. For s = 0.5m, half of the downfield VAWT is exposed to the wake regions of the leading row of VAWTs. This resulted in a power output for the downfield VAWT that was approximately 15.4-22.2% lower than the power for a VAWT in a two turbine array with the same spacing. This effect is shown below in Table 5.

Table 5. Power vs x_{DF} for s = 0.5m and m = 20

x_{DF}	0m	0.5m	1m	1.5m	2m	2.5m	3m	3.5m
Power (W/l)	885.4	881.3	873.6	866.7	860.2	858.1	854.0	813.9
Change in power	-15.4%	-15.7%	-16.5%	-17.2%	-17.8%	-18.0%	-18.4%	-22.2%

Note. The change in power is for the downfield VAWT relative to the power of a VAWT in two turbine arrays for the same spacing

The velocity contours for s = 0.5m and x_{DF} = 0.5m with m = 20 is shown in Fig. 40.

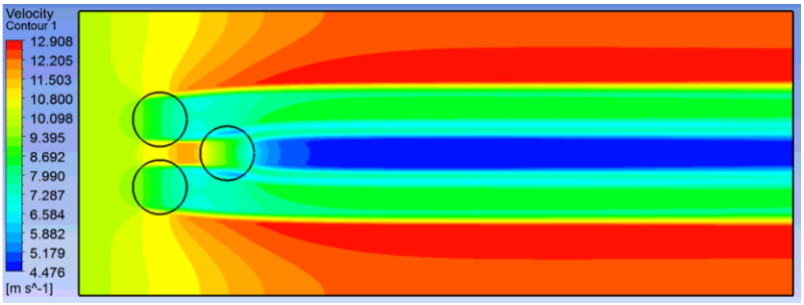

Figure 40. Velocity contours for ideal case with s = 0.5m, x_{DF} = 0.5m

A similar effect is seen with s = 1m, however, for this case only 25% of the downfield VAWT is exposed to the wake regions as shown in Fig. 41.

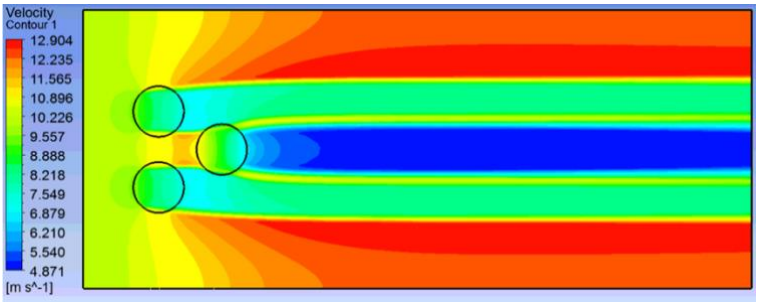

Figure 41. Velocity contours for ideal case with s = 1m, x_{DF} = 0.5m

The remaining 75% of the downfield VAWT was exposed to regions of increased velocity. As such, the power of the downfield VAWT was higher than the power for a VAWT in a two turbine array. This is shown in Table 6 for each downfield spacing.

Table 6. Power vs x_{DF} for s = 1m and m = 20

x_{DF}	Even	0.5m	1m	1.5m	2m	2.5m	3m	3.5m
Power (W/l)	1128.5	1129.3	1125.8	1121.2	1117.5	1114.6	1111.2	1109.0
Change in power	8.91%	8.99%	8.65%	8.21%	7.86%	7.57%	7.25%	7.04%

Note. See Table 5

For s = 2m, the spacing and actuator cylinder diameter were equal and at no point was the downfield VAWT exposed to the wakes of the leading row. This resulted in the highest power for the four primary cases addressed above. Velocity contours for this case is shown in Fig. 42.

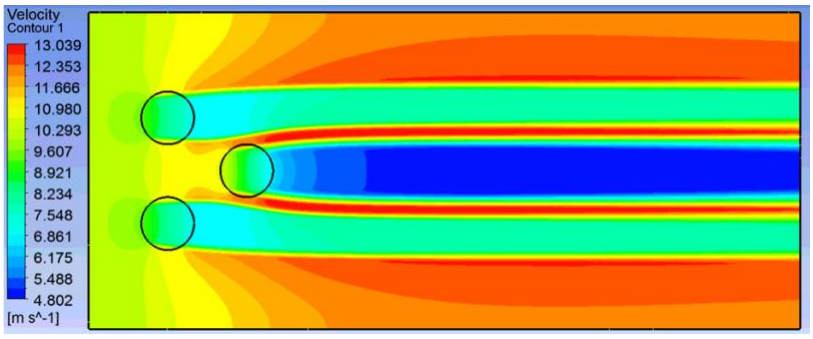

Figure 42. Velocity contours for ideal case with s = 2m, x_{DF} = 0.5m

By avoiding regions of wake overlap, a maximum induced velocity of 13.039m/s resulted. Similar to the case for s = 1m, the power for the downfield VAWT was higher than the power for a VAWT in a two turbine array for the same spacing. In this case, the percent increase was significantly higher, ranging from 18.8-21.0%. Change in Power with x_{DF} for s = 2m and m = 20 is given in Table 7.

Table 7. Power vs x_{DF} for s = 2m and m = 20

x_{DF}	Even	0.5m	1m	1.5m	2m	2.5m	3m	3.5m
Power (W/l)	1225.1	1233.9	1230.0	1228.2	1222.4	1222.8	1214.5	1211.5
Change in power	20.2%	21.0%	20.7%	20.4%	19.9%	19.9%	19.1%	18.8%

Note. See Table 5

While regions of wake overlap are also avoided for s = 4m, the wider spacing also meant that the interactions outside of the wake were between regions with lower velocity magnitudes. This is similar to the results from the two VAWT arrays. The freestream velocity at the head of the actuator cylinder was also lower for s = 4m. As can be seen in Fig. 43, the velocity at the head of the actuator cylinder was approximately 10% less than the case for s = 2m.

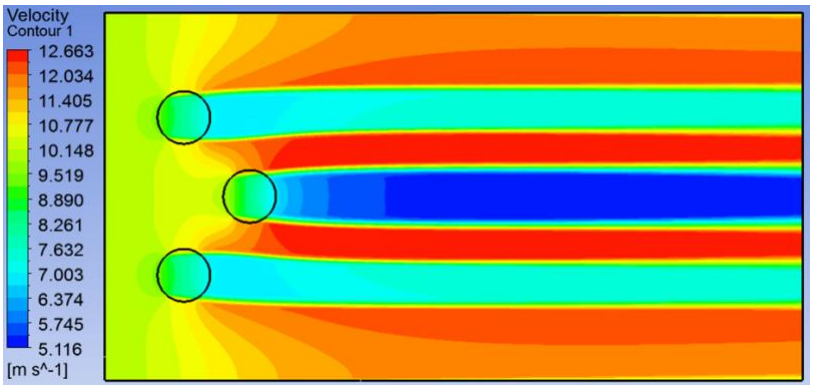

Figure 43. Velocity contours for ideal case with s = 4m, x_{DF} = 0.5m

While the power of the downfield VAWT was still higher than a VAWT in a two turbine array for the same spacing, the percent increase for s = 4m was approximately 25% of the increase observed for s = 2m. The change in power for higher spacing was also observed to be far less pronounced for each variation in x_{DF} as shown in Table 8. This is a result of the more uniform profile at the leading edge of the actuator cylinder.

Table 8. Power vs x_{DF} for s = 4m and m = 20

x_{DF}	Even	0.5m	1m	1.5m	2m	2.5m	3m	3.5m
Power (W/l)	1051.0	1056.9	1056.6	1055.5	1052.7	1051.2	1047.4	1045.2
Change in power	5.06%	5.66%	5.63%	5.52%	5.23%	5.08%	4.71%	4.49%

Note. See Table 5

4.3.3 Downfield VAWT Refinement Cases

To further optimize the power output of the downfield actuator cylinder, a series of refinement cases were performed around s = 2m. The refinement cases were once more limited to the ideal VAWT with m = 20. Trials were first conducted for s = 1.75m and s = 2.25m. These results are included below in Table 9.

Table 9. Refinement study for downfield VAWT in three VAWT array

	Power (W/l)							
x_{DF}	Even	0.5m	1m	1.5m	2m	2.5m	3m	3.5m
s = 2.25m	1015.8	1011.6	1009.7	1009.0	1009.1	1009.3	1009.7	1010.0
s = 1.75m	1189.9	1196.7	1195.6	1191.8	1187.5	1183.5	1180.1	1177.4

As can be seen above, the downfield VAWT for s = 1.75m outperformed the downfield VAWT for s = 2.25m for each variation of x_{DF}. Furthermore, by comparing the results to Table 7 for s = 2m, the downfield VAWT with s = 1.75m also outperformed s = 2m. This result indicates that a spacing less than the diameter of the downfield VAWT may in fact be optimum despite the potential exposure to the wake regions of the leading row of VAWTs. By examining the velocity contours, it can be observed that for $s < D$ it is possible for the wake profile of the leading row to contour around the downfield VAWT. This is shown below in Fig. 44 for s = 1.75m and x_{DF} = 0.5m.

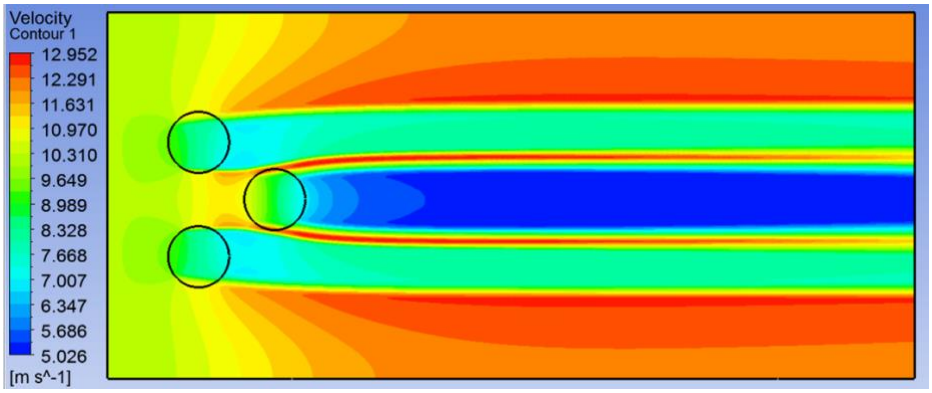

Figure 44. Velocity contours for ideal case with s = 1.75m, x_{DF} = 0.5m

The induced velocity around the wake profile of the downfield VAWT displaces the wake of the leading row of VAWTs. To further examine this effect, additional cases were implemented for s = 1.5m and s = 1.25m.

A similar result to s = 1.75m was found for s = 1.5m. As seen in the velocity contours in Fig. 45 below, the wakes of the leading actuator cylinders contoured around the pressure jump and wake profile of the downfield actuator cylinder.

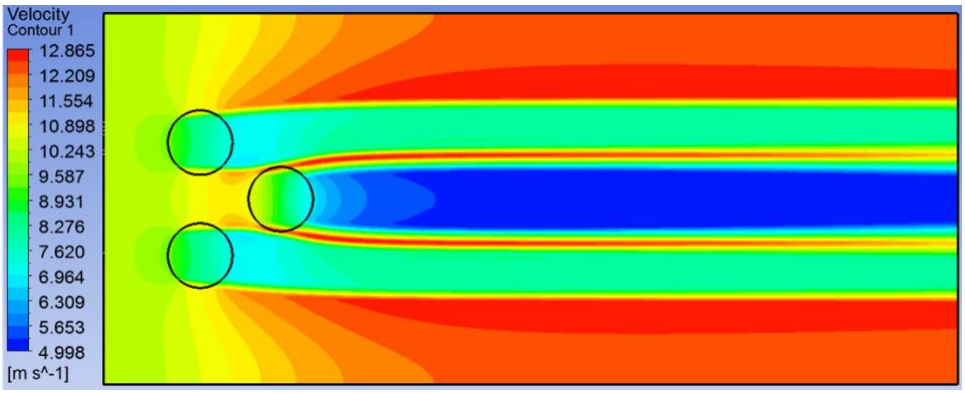

Figure 45. Velocity contours for ideal case with s = 1.50m, x_{DF} = 0.5m

This has a positive impact on power output; the downfield VAWT for s = 1.5m outperformed the downfield VAWT for both s = 2m and s = 1.75m. For s = 1.25m, the power output was still greater than s = 2m but it was less than the cases for s = 1.75m and s = 1.5m. As seen in the velocity contours in Fig. 46, while there was slight contouring about the downfield profile, the exterior of the actuator cylinder was still incident to the wakes of the leading row of VAWTs.

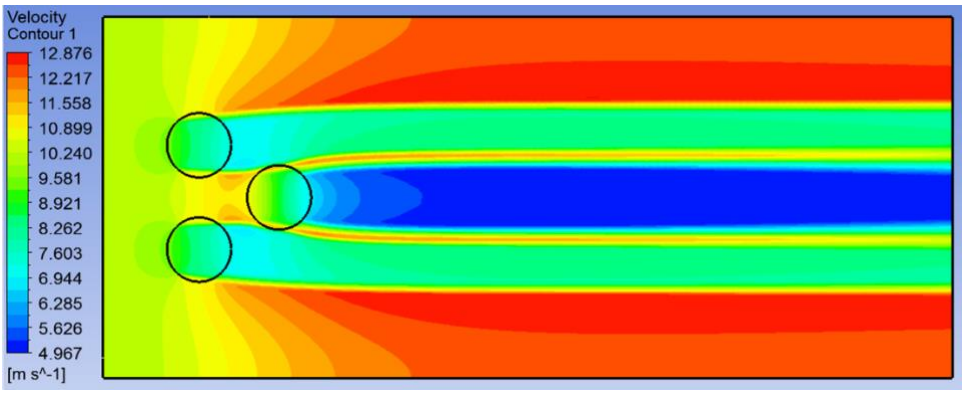

Figure 46. Velocity contours for ideal case with s = 1.25m, x_{DF} = 0.5m

The power for both s = 1.5m and s = 1.25m is included in Table 10 below.

Table 10. Refinement study for downfield VAWT in three turbine array

	Power (W/l)							
x_{DF}	Even	0.5m	1m	1.5m	2m	2.5m	3m	3.5m
s = 1.5m	1296.0	1287.2	1271.9	1270.9	1262.3	1260.0	1261.6	1252.6
s = 1.25m	1234.2	1233.5	1229.0	1223.6	1218.6	1215.6	1212.2	1211.4

4.3.4 Comparisons of Three VAWT Geometries

In order to compare the complete three VAWT arrays, the power output of the leading row of VAWTs needed to be considered in addition to the downfield VAWT. For this analysis, an additional set of calculations were repeated for the leading row of VAWTs to determine if the presence of the downfield VAWT had any effect on their power output. Identical geometries and boundary conditions were used; however, the coordinate axes were realigned to coincide with the bottom turbine of the first row of VAWTs rather than the downfield VAWT.

For each spacing variation, the power of a VAWT in the leading row for three VAWT arrays was plotted versus the power of a VAWT in a two VAWT array. For cases with $s \leq$ R, the power for the leading row of VAWTs was found to be directly related to x_{DF}. This means that the power of the leading row was most negatively affected for a tightly packed VAWT array with x_{DF} = 0m. This is shown below in Fig. 47for s = 0.5m and s = 1m.

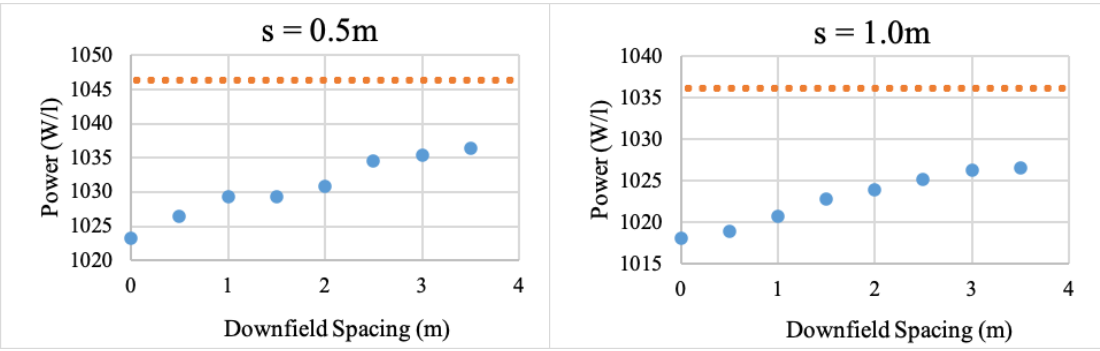

Figure 47. Power of VAWT in leading row for two and three turbine arrays for $s \leq R$

For s = 0.5m, the front row of VAWTs decreased in power by as much as 2.21% each. For s = 1m, the front row of VAWTs decreased in power by as much as 1.75% each, as compared to a two VAWT array with identical spacing. As x_{DF} increased, the power of the leading row of VAWTs became less affected by the downfield actuator cylinder and approached he same power as the two VAWT array. This result is a required consequence for the model; for large x_{DF}, the presence of downfield VAWT should become negligible.

As s increases the same general trend is observed; however, the behavior for small x_{DF} becomes highly dependent on the spacing. For $R < s < D$, the power of the leading row of VAWTs experienced a temporary peak for the even alignment with x_{DF} = 0m before decreasing and returning to the original trend observed in Fig. 48. This is shown below for s = 1.5m and s = 1.75m.

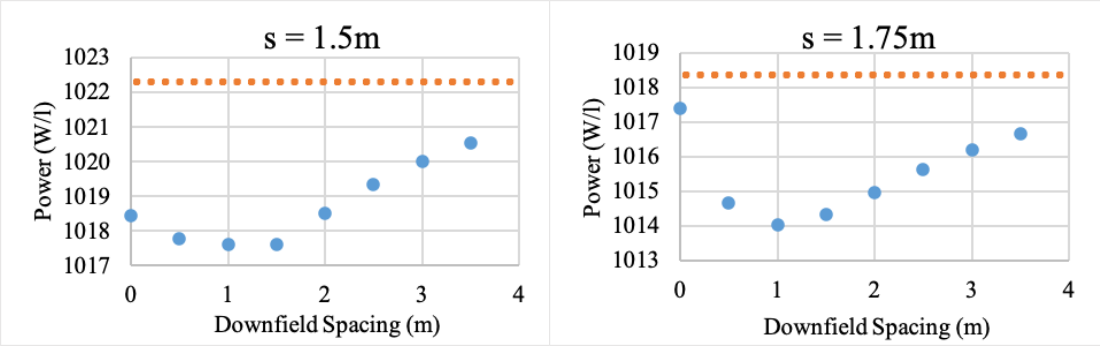

Figure 48. Power of VAWT in leading row for two and three turbine arrays for $R < s < D$

As spacing increased, the downfield VAWT had a reduced effect on the leading row. For s $\geq D$, the relationship between power and downfield spacing was initially inversely related and appeared to rebound at a greater distance downfield. This is shown in Fig. 49 for s = 2m and s = 4m.

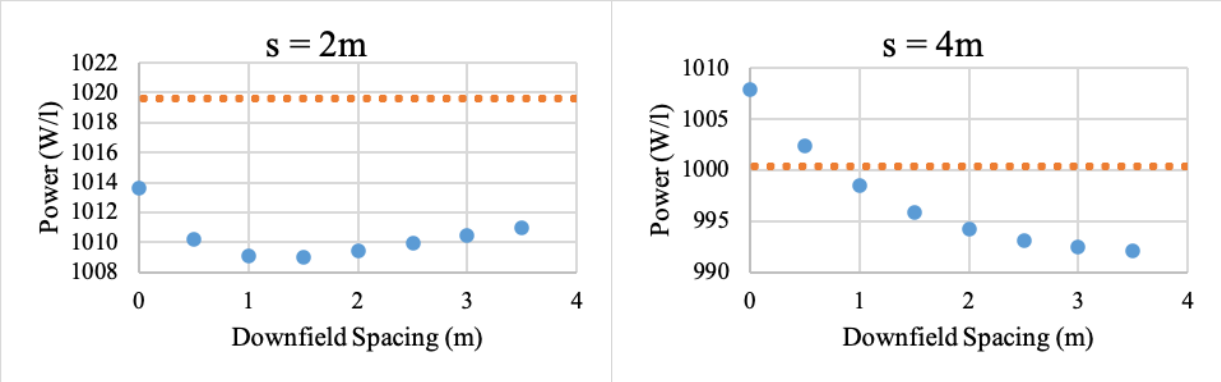

Figure 49. Power of VAWT in leading row for two and three turbine arrays $s \geq D$

While there appears to be slight difference in behavior that may rebound as x_{DF} increases, for $s \geq D$ the difference between the leading row of VAWTs for two and three turbine cases remained within 0.75% at all times. Additional cases for larger x_{DF} may demonstrate further rebounding in power toward the two VAWT array.

Using the results above, power was calculated for each combination of s and x_{DF}. While the downfield position contributed to differences in power for individual VAWTs, the differences were very slight when considering the entire array. For each spacing, the power of the leading row typically increased with x_{DF} while the power of the downfield VAWT decreased with x_{DF}. The decrease in power associated with the downfield VAWT was always larger than the increase in power associated with the front row of VAWTs. However, in either case, each factor mitigated the effect of the other. The percent difference between any system due to x_{DF} varying from 0m to 3.5m was never greater than 1.65% of the total power output for a three VAWT array. The spacing of the leading row was found to be the primary distinguishing factor. Furthermore, as the maximum power for each spacing variation occurred at a downfield position between x_{DF} = 0 and x_{DF} = 1, a tighter downfield spacing was found to be beneficial both in terms of power output and required land area. In Fig. 50 below, maximum power is plotted for each spacing.

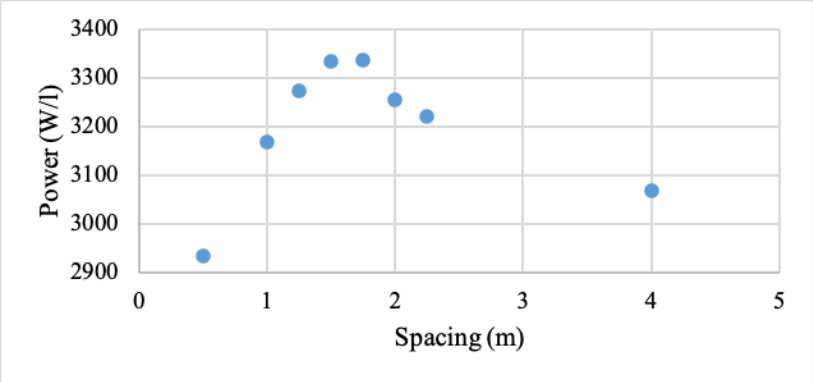

Figure 50. Maximum power for three VAWT arrays as a function of *s*

The power increased to a maximum near 1.5m to 1.75m; this is representative of a spacing equal to 0.75D-0.875D. For the spacing of 1.75m, the maximum power output for all arrays was achieved at x_{DF} = 0.5m. The power for s = 1.5m at x_{DF} = 0m was also within a tenth of a percent.

For the application of extended VAWT arrays, the consideration of land area becomes increasingly important. However, for this analysis, the primary focus was for vertical spacing of two to three VAWT clusters. The arrays may be extrapolated for large distances in the y-direction, however further analysis is required to determine the optimum downfield position of the next row of VAWTs. For the domains of the two and three VAWT arrays, there were not significant differences found in the recovery rate of the downfield velocity to make definitive conclusions about which combinations of *s* and for x_{DF} were most advantageous in that regard.

In considering only the vertical spacing of VAWT arrays, a quasi-power density can be computed. For this analysis, the total system power is divided by the immediate land area required for the three actuator cylinders. Here the area can simply be calculated as:

$$A = (2R + s)(2R + x_{DF}) \tag{9}$$

Using this approximation for power density, the following trend was found.

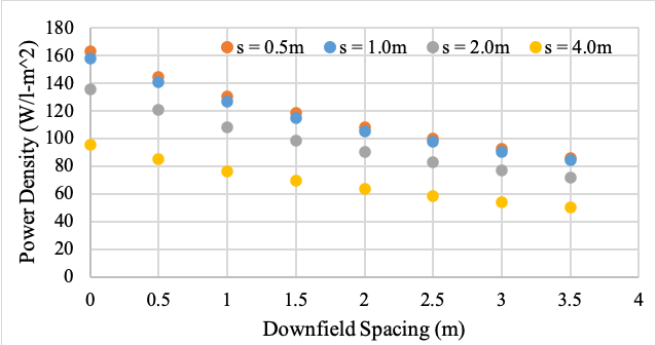

Figure 51. Quasi power density for three VAWT arrays as a function of s and x_{DF}

As can be seen from Fig. 51, while power output was frequently higher for cases with x_{DF} = 0.5m or x_{DF} = 1m, the increase in power was not proportional to the increase in required land area for each s variation. This indicates that the even alignment of the downfield VAWT is the most efficient despite slight sacrifices in power. A similar trend is observed by comparing s for constant x_{DF}. This is shown below in Fig. 52 for x_{DF} = 0m.

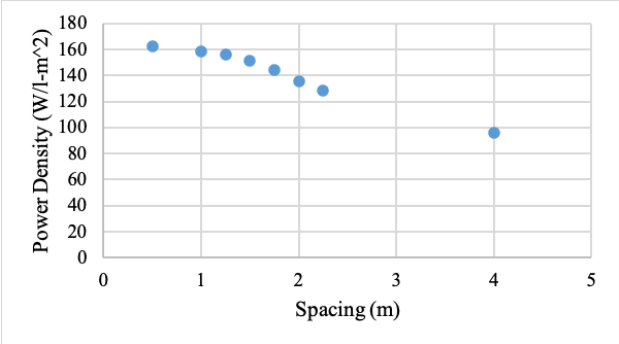

Figure 52. Quasi power density vs. s

Despite arrays with higher values for s producing as much as 10% more power, the case for s = 0.5m had the greatest power density. This suggests that more tightly packed arrays are advantageous; however, as previously stated this analysis does not take into account the required downfield distance for the next row. Further analysis is required to determine if any substantial variation exists for velocity recovery downfield using the Actuator Cylinder Model. Additionally, for VAWTs with s < D, the model does not consider a real VAWTs ability to

perform with large gradients in V_∞ depending on y-position. As displayed in Fig. 30, the power of the downfield VAWT is enhanced by a small center region of increased velocity. While this region is able to partially compensate for losses in the remaining regions that are exposed to the wakes, it is unclear how this would affect the VAWTs ability to rotate when a finite number of blades are considered.

4.3.5 Conclusions

Based on the two and three actuator cylinder study, the following conclusions can be drawn:

(1) Based on the Actuator Cylinder Model, narrow spacing is ideal for a two VAWT array. Compared to an isolated VAWT, the power output of an ideal VAWT in a pair can be increased by up to 5-6% due to region of elevated velocity directly outside of the wake.

(2) So long as the downfield VAWT is not placed in the immediate wake of a VAWT in the leading row, a three VAWT array is advantageous to a two VAWT array. Due to the increased velocity outside of the wake, the downfield VAWT typically has the largest power output of any VAWT in the array.

(3) For a three VAWT array, the front row spacing has a greater effect on power than the downfield distance. To optimize the power of the downfield VAWT the spacing should be in the range of 0.75D-0.875D.

(4) While the maximum power output for a three VAWT array occurs for s = 0.75D-0.875D and x_{DF} = 0.25D-0.5D, the losses in power associated with narrower spacing are proportionally less than the decrease in required area. This suggests that VAWTs packed as tightly as possible are advantageous; however, to calculate a true power density using the Actuator Cylinder Model the optimum downfield distance of the next row of VAWTs must be determined. Effects associated

with a non-uniform velocity at the head of the downfield VAWT for a finite number of blades should be investigated.

Chapter 5: Airborne Wind Energy Application

5.1 Background

The relationship between power and wind speed is cubic. This is shown using the Actuator Cylinder Model in Fig. 17. Since winds are stronger and more consistent at high altitudes, the design of wind turbines is becoming increasingly taller. The average hub height of commercial wind turbines in the United States is now over 80m [16]. While there are still efforts to design and build larger wind turbines, there are practical limits to tower height both structurally and economically.

In recent years, a number of airborne wind energy applications have been suggested as alternate means to harness winds at even higher altitudes. Not only do airborne applications provide the potential to reach higher wind speeds, but they also eliminate substantial material costs since there is no need for large towers. One design type that has garnered significant attention is tethered wind turbines. Tethered wind turbines incorporate a high-altitude mechanism connected to a ground station via tensioned cables. For many designs, the high-altitude mechanism is a kite system [17]. For such systems, a fraction of the power is sacrificed to generate lift, other energy is lost due to counter cable tensioning, and the remaining energy is transmitted down the wiring to the ground [18].

One variation of tethered wind turbines is a design featuring a quadcopter drone. One prominent example is the Flying Electric Generator (FEG) from Sky WindPower Corporation [19]. For this concept shown below in Fig. 53, the rotors are used to both lift the device and generate added energy which is transmitted down the tether [19].

Figure 53. Sky WindPower design concept and prototype for Flying Electric Generators [19]

5.2 Airborne Application Concept Development

For the analysis using the Actuator Cylinder Model, a similar design concept will be utilized, however rather than analyze a quadcopter with variable rotor tilt that is responsible for maintaining elevation and generating power, the sole function of the quadcopter is assumed to be to suspend reduced scale VAWTs. The initial power associated with the quadcopter is also assumed to be sufficient enough to get the device to the goal elevation before relying on the VAWT array to provide continuous power to hover. A free body diagram for the system is shown in Fig. 54.

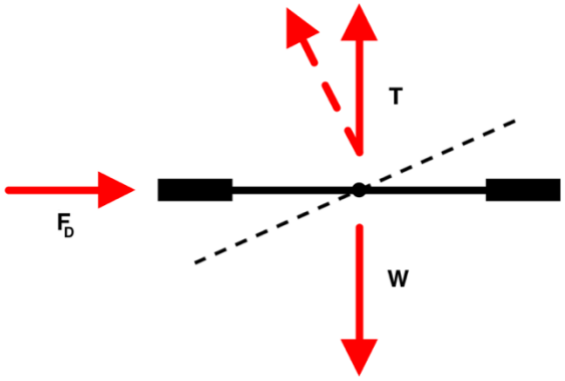

Figure 54. Airborne VAWT free body diagram [20]

As can be seen in Fig. 54, the forces of consideration are the weight due to gravity, a drag force from the wind, and a stabilizing thrust vector. The initial focus is to ensure that the quadcopter

can account for the entire weight of the system and still produce excess energy. The drag force is neglected and the thrust is considered to be solely in the vertical direction opposite gravity. For the diagram above, the VAWT array is simplified as a centered point mass. This assumption is valid so long as the VAWTs are in the same plane and the spacing is symmetric about the center point. For the inclusion of a drag force, tilting the rotors would be required to maintain equilibrium in both the x and y directions. To implement the Actuator Cylinder Model in such a system, it would also require that only the rotors be tilted while the body of the quadcopter remains level. This would keep the VAWTs vertically aligned at all times.

To estimate the weight of each VAWT, comparisons were made with commercial straight-bladed VAWTs and then scaled accordingly. The following design parameters given in Table 11 were utilized.

Table 11. Design parameters for straight blade H-Type VAWT

Number of Blades	Chord length (m)	Radius (m)	Aspect Ratio
3	$7.8125 \cdot \mathbf{10^{-4}}$	0.25	4

Note. VAWT parameters scaled proportionally from experimental trials seen in [21]

For $c = 7.8125 \cdot 10^{-4}$m and $AR = 4$, a resulting blade height of 0.3125m can be obtained. For this size, a total VAWT mass was calculated to be roughly 7kg each. For a payload of 14k-21kg for two and three VAWTs, a quadcopter weight near 40kg is typical [22]. The operational height for the WindPower FEGs is 200m to 600m [19]. To be within this range, a height of 500m was selected for this analysis. At this altitude, the density of air is 1.167 kg/m3 [23].

For wind speeds at 500m, power law was used with wind data from 50m and 80m to extend the vertical wind speed profile [24]. For power law, the wind speed at a height z is found using a known wind speed from a reference height z_R.

$$U(z) = U(z_R) \cdot \left(\frac{z}{z_R}\right)^{\alpha} \tag{10}$$

As can be seen in Eq. 9 above, the two wind speeds are related through a coefficient α. Several methods have been utilized to determine proper values of α; for this application, a correlation based on velocity and height is used [24].

$$\alpha = \frac{0.37 - 0.88 \ln U(z_R)}{1 - 0.088 \ln \frac{z_R}{10}} \tag{11}$$

For the reference wind data, only the ideal case for a wind power class of 7 is considered. For an altitude of 50m, locations that are wind power class 7 tend to exhibit average wind speeds near 11.9m/s [25]. For some sites annual wind speed averages can be even higher and approach 15m/s at elevations of 80m [26]. Using power law with this data, annual averages at 500m were calculated to be 17.9m/s to 21.1m/s. However, it should be noted that this calculation is for an entire year. Airborne wind applications can be selectively deployed at times with peak wind conditions. Depending on factors such as time of day or month in the year, wind speeds can be considerably higher than the annual average [26]. As such, rather than use a wind speed for an average near 20m/s, more optimized conditions for 30m/s, 40m/s, and 50m/s will be considered.

Using these reference conditions, the required thrust and power were calculated in two parts; first for the ascension to 500m, and then for the power required to maintain that height. For a purely vertical ascension, Newton's 2nd law yields:

$$\sum F_y = T - W = m \cdot a \tag{12}$$

To calculate the power required to hover at 500m, $a = 0$ is applied since the system is assumed to be in equilibrium. Ideal power can then be found by taking the product of thrust and velocity [2].

$$P = T \cdot v \tag{13}$$

For Eq. 12, the velocity is the induced velocity across the rotors of the quadcopter [27]. Assuming equal conditions for each rotor, 1D Momentum Theory can be applied. Here the application of an actuator disk is suitable since each rotor axis is parallel to the external flow. By

applying the principle of conservation of momentum to a vertical variation of the control volume shown in Fig. 3, the induced velocity across the rotor has the form

$$U_{2,3} = \sqrt{\frac{T}{2 \cdot \rho \cdot A}} \tag{14}$$

Substituting this relation into Eq. 12 yields an expression for power depending only on the thrust and rotor area of the quadcopter [27].

$$P = \frac{T^{3/2}}{\sqrt{\rho \cdot A}} \tag{15}$$

In this form the thrust is equal to the weight and *A* is the total area across all rotors. For this system, the area is estimated by using four identical rotors with D = 0.5m [22].

Newton's 2nd law is applied once more for the climb to 500m. For this case the acceleration is no longer zero; however, it is the only unknown when neglecting the drag force. The acceleration can easily be found using the definition of velocity in conjunction with the following kinematic equation:

$$y = y_o + v_{0,y} \cdot t + \frac{1}{2} \cdot a \cdot t^2 \tag{16}$$

For a start from rest at ground level, y_o and $v_{0,y}$ are zero. Then by assuming an ascent velocity of 3m/s, *t* and *a* can readily be found and used to calculate the thrust. For this case the induced velocity in Eq. 11 must be reformulated to include the ascent speed. This is shown below in Eq. 16.

$$P = T \cdot (v + v_y) \tag{17}$$

where v_y is the ascent velocity. By distributing *T*, it can be observed that

$$P = T \cdot v + T \cdot v_y \tag{18}$$

This indicates that the power required to climb to 500m is equal to the power required to hover plus an additional quantity dependent on ascent rate.

5.3 Airborne Application Physical Model and Grid

Geometries for two and three VAWT models were created. For two VAWTs, the same methods used in Fig. 27 were used to generate the computational domain. From the previous analysis, a narrow spacing was determined to be beneficial. As such, a geometry with s = 0.125m and D = 0.5m was constructed by scaling the 2m diameter case with s = 0.5m by a factor of 1/4. For the three VAWT design, the actuator cylinders were evenly spaced 60° apart. Since s = 0.875D had the maximum output from the previous 3 VAWT investigation, s = 0.4375m was used with D = 0.5m. This corresponds to x_{DF} = 0.312m. For each case the same mesh parameters, boundary conditions, SimpleC numerical algorithm, and convergence criteria from the previous methods were applied.

5.4 Airborne Wind Energy Results and Discussion

5.4.1 Concept Evaluation using Actuator Cylinder Theory

To evaluate each system, power from each quadcopter was compared to the power required to climb to 500m and to maintain that elevation. For each freestream velocity variation, power was calculated using the methods shown in Eq. 7. For this calculation the power is per unit length; as such, the power of each VAWT was then multiplied by blade height of 0.3125m to get the total output. The required power for the two VAWT system is included in Table 12 below.

Table 12. Power requirements for two VAWT airborne application

System weight (N)	Power required to climb (W)	Power required to hover (W)	Total required power (W)
529.7	6097.7	4502.7	10600.4

Note: Drag forces were neglected for both vertical ascent and for hovering at 500m

Using this result, power comparisons were made for each variation in freestream velocity as given in Table 13.

Table 13. Power comparisons for two VAWT airborne application

Freestream velocity (m/s)	Power generated (W)	Total output (W)
30m/s	4213.4	-6387.0
40m/s	9987.3	2024.5
50m/s	19506.2	8905.9

Note: Total output is computed as the difference between power generated and total required power from Table 12

As can be seen above, for V_∞ = 30m/s more power was required than generated. For this case the application is not viable. For V_∞ = 40m/s and V_∞ = 50m/s, positive outputs were observed. However, for 40m/s the output was relatively low when considering that the case was modeled for an ideal VAWT under ideal external conditions. The drag forces were also neglected for each case; this is also why the required power is the same across each freestream velocity. By observing Eq. 5 which equates Δp_{max} to the drag force over the swept area, the drag force is seen to change proportionally to V_∞^2. This means that greater losses will occur when incident to freestream velocities of higher magnitude. For airborne altitudes applications with high freestream velocities the drag force can become substantial if the design of the quadcopter is not streamlined. For higher values of C_D, the assumption to neglect the drag force introduces substantial error.

The power requirements for a quadcopter with 3 VAWTs are shown in Table 14.

Table 14. Power requirements for three VAWT airborne application

System weight (N)	Power required to climb (W)	Power required to hover (W)	Total required power (W)
598.4	7265.8	5406.0	13271.8

Note: Drag forces were neglected for both vertical ascent and for hovering at 500m

With the added mass from the third VAWT, the total required power increased by 25.2%. The total output for this case is shown in Table 15.

Table 15. Power comparisons for three VAWT airborne application

Freestream velocity (m/s)	Power generated (W)	Total output (W)
30m/s	6,741.1	-5930.7
40m/s	15,979.4	3307.6
50m/s	31209.7	18537.9

Note: Total output is computed as the difference between power generated and total required power from Table 12

Once more, the case for V_∞ = 30m/s was shown to be unviable and cases with wind speeds close to 50m/s demonstrated promise. Furthermore, by comparing the results from Table 15 to Table 13, it can be observed that the addition of the third VAWT was beneficial across each freestream velocity. Since the drag forces are neglected, this result can be attributed to the ratio of power to weight. While the mass and total required power go up for a third VAWT, the capacity for power generation increases at a higher rate proportionally. This is in large part due to the estimates for the VAWT and the quadcopter masses. The quadcopter mass is just under 6 times the approximate mass of a VAWT; thus, by adding a VAWT the mass only increases by 10.9%. Comparatively, the output increases by over 33% since the downfield VAWT has the highest generated power in the array.

5.5 Recommendations for Future Work

Results can vary significantly based on the required payload and drag coefficient of the model. Additional cases should be considered for a range of quadcopter weights relative to VAWT weights. The estimates used in this analysis were for standard commercial VAWTs; a greater focus should be placed on reducing the weight of the system through the material selection.

An additional area of consideration that was neglected in this analysis is the added moment from the rotation of the VAWTs. This principal is considered for the design of all rotor powered aircrafts and is the reason that there is typically a symmetric design with counter rotating pairs. For controlled rotor systems, it is also possible to eliminate a moment by setting variable rotor speeds, tilting rotor blades, or implementing level arms of different lengths. For free rotating VAWTs, this is much more difficult to achieve and is in large part controllable only through rotor direction.

For two VAWT concepts, it is possible to avoid the addition of a moment by using counter rotating pairs. This is demonstrated in the diagram on the left in Fig. 55.

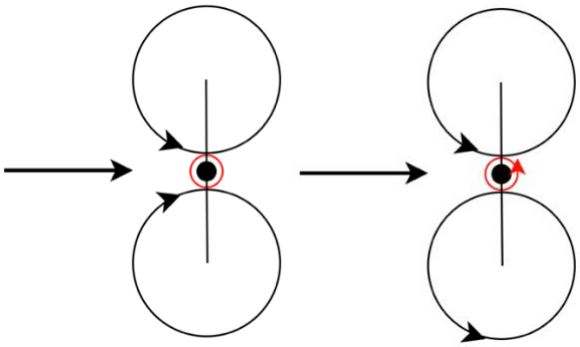

Figure 55. Pair of VAWTs for counter and co-rotating cases

Assuming an equal rotational velocity, the added moment of the top and bottom VAWTs will cancel out. For the co-rotating case shown on the right, the added moment of each VAWT will result in a nonzero total moment for the connected system of VAWTs.

For a three VAWT system, an added moment must always be considered. As can be seen in Fig. 56 below, while the magnitude will vary depending on which VAWTs rotate in which direction, a moment imbalance will always be present.

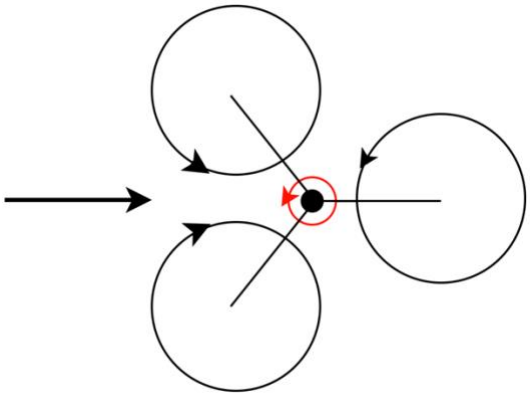

Figure 56. Moment resulting from three VAWT array

While this principal is not included in the development of the Actuator Cylinder Model and is thus not reflected in flow behavior, it is an important consideration for the airborne application.

5.6 Conclusions

Based on the analysis of the airborne wind application, the following conclusions can be drawn:

(1) For the design to be viable, wind speeds must be greater than 30m/s and likely between 40-50m/s or greater when including the drag force.

(2) The output for the quadcopter is heavily dependent on the mass of the system. By optimizing the materials used in the VAWTs it is possible to reduce the mass of the quadcopter and in turn require a lower wind speed to net a positive power output.

(3) The results of this simplified analysis indicate that three VAWT arrays are superior to two VAWT arrays in terms of power generation capabilities for airborne applications, however a moment will be generated by adding free rotating VAWTs. For a design with two VAWTs, the VAWTs should be counter-rotating. For a three or more VAWTs it will be increasingly difficult to counteract the moment without additional design considerations.

References

[1] International Energy Agency Report, “Renewables Analysis and Forecast to 2024,” 2017.

[2] Manwell J.F., McGowan J.G., Rogers A.L., Wind Energy Explained: Theory, Design and Application, Wiley, 2009, Chapter 1, pp. 11-34.

[3] Crossley, R., P. Schubel, “Wind Turbine Blade Design.” Energies, Vol. 5, 2012, pp. 3425-3447.

[4] J. Meyers, C. Meneveau, “Optimal turbine spacing in fully developed wind farm boundary layers." *Wind Energy*, Vol. 15, 2012, pp. 305–317.

[5] B. Sørensen, Renewable Energy: Its Physics, Engineering, Use, Environmental Impacts, Economy, and Planning Aspects, Elsevier, 2004.

[6] European Wind Energy Association, “Wind Energy Basics," 2016.

[7] Hazaveh, S., et all, “Increasing the Power Production of Vertical-Axis Wind-Turbine Farms Using Synergistic Clustering,” Boundary Layer Meteorology, Vol 169, 2018, pp. 275-296.

[8] Battisti, L., Gli Impianti Motori Eolici, Battisti Editore, 2012.

[9] Wilkie, J., Leithead W.E., and Anderson, C., “Modeling of Wind Turbines by Simple Models,” Wind Engineering, Vol. 4, 1990, pp. 247-274

[10] Manwell J.F., McGowan J.G., Rogers A.L., Wind Energy Explained: Theory, Design and Application, Wiley, 2009, Chapter 2, pp. 117-121.

[11] Madsen H., “The Actuator Cylinder: A Flow Model for Vertical Axis Wind Turbines,” PhD Thesis, Aalborg University, Denmark, January 1982.

[12] ANSYS®, Release 12.0, Theory Guide - Spalart-Allmaras Model, 4.3, 2009.

[13] ANSYS®, Release 11.0, Theory Guide - Spalart-Allmaras Model, 18.3, 2009.

[14] Blandford, R. and Thorne, K., Applications of Classical Physics, 2013, Chapter 14.

[15] Dabiri J., “Potential Order-of-Magnitude Enhancement of Wind Farm Power Density via Counter-Rotating Vertical-Axis Wind Turbine Arrays,” AIP J. of Renewable and Sustainable Energy, Vol. 3, 2011, p. 043104.

[16] International Energy Agency Report, “Wind turbine heights and capacities have increased over the past decade,” 2017.

[17] Yoshida, S. et al. “Hardware-in-the-Loop (HIL) and Experimental Findings for the 7kW Pumping Kite Power System.” AIAA Scitech 2020 Forum, pp. 3-12.

[18] Peters, D. et al. “Optimum Operational Parameters for Tethered Yawed Wind Turbines.” AIAA Applied Aerodynamics Conference, 2011-3372.

[19] Sky WindPower Corporation. Sky WindPower Executive Summary December 2018, pp. 1-2.

[20] Uehara, D., “Energy Modeling of VTOL Aircraft for Titan Aerial Daughter craft (TAD) Concepts,” IEEE Aerospace Conference, 2019.

[21] Feng, F. et al. “Research on Aerodynamic Characteristics of Straight-Bladed Vertical Axis Wind Turbine with S Series Airfoils,” International Journal of Rotating Machinery, Vol. 2018, A. 8350243.

[22] Alta. (2020, April 15). Retrieved from https:freeflysystems.com/alta

[23] Borgnakke, C., Sonntagg, R.E., Fundamentals of Thermodynamics, Wiley, 2013, Appendix A,2pp 760-763.

[24] Manwell J.F., McGowan J.G., Rogers A.L., Wind Energy Explained: Theory, Design and Application, Wiley, 2009, Chapter 2, pp. 36-47.

[25] National Renewable Energy Laboratory, “Wind Energy Resource Atlas of the U.S,” 2010.

[26] Archer, C., and Jacobson, M., “The Spatial and Temporal Distributions of U.S. Winds and Wind power at 80 m Derived from Measurements,” Journal of Geophysical Research, Atmospheres, 2002.

[27] Rotauru, C., and Todorov, M., Flight Physics Models, Techniques and Technologies, InTech, 2018, Chapter 2, pp. 19-28.

Appendix A: Chapter 2 Figures and Data

A1: Figures from mesh refinement study

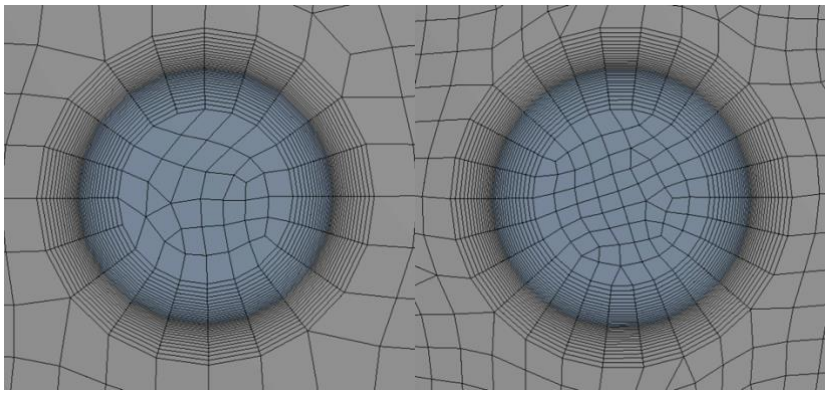

Figure A1. Mesh #1 (left) and Mesh #2 (right)

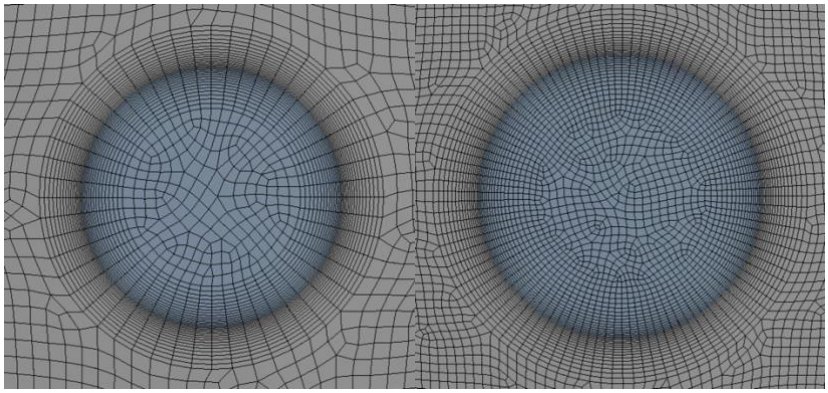

Figure A2. Mesh #3 (left) and Mesh #4 (right)

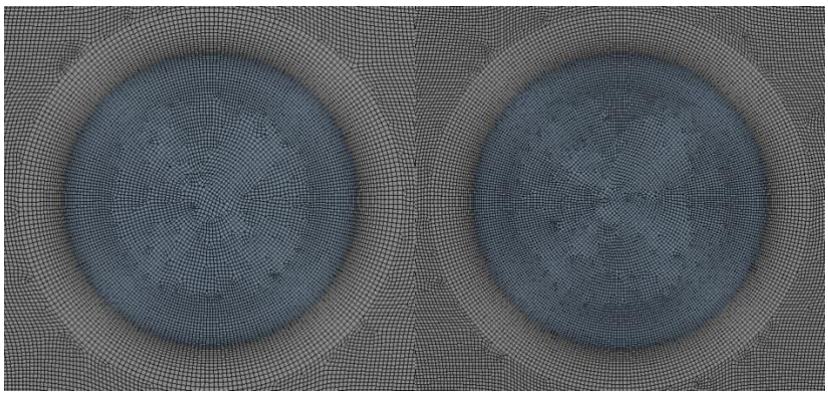

Figure A3. Mesh #6 (left) and Mesh #7 (right)

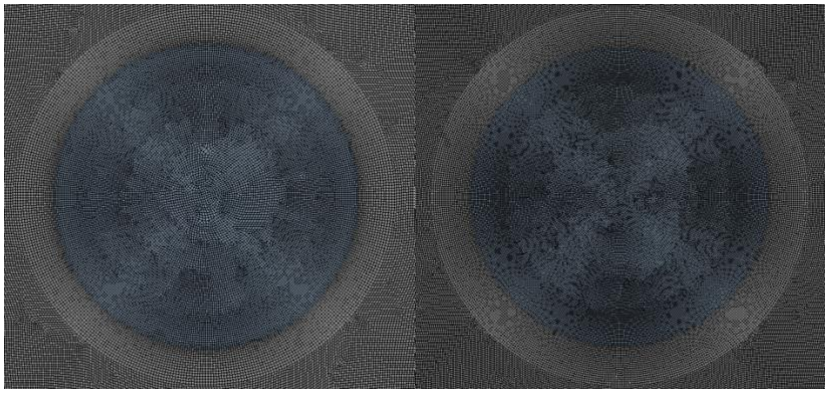

Figure A4. Mesh #8 (left) and Mesh #9 (right)

A2: Comparison of numerical algorithms

Table A1. Comparisons for Coupled, Simple, and SimpleC algorithms for D = 1m, V_∞ = 1m/s

Coupled		Simple		SimpleC	
Power (W/l)	Cp	Power (W/l)	Cp	Power (W/l)	Cp
1.046131	0.426992	1.046322	0.42707	1.046282	0.42705

Note: Mesh #5 used for this analysis

Appendix B: Chapter 3 Figures and Data

B1: Comparisons for freestream velocity, *m*, and output

Table B1. Power vs. m for series of freestream velocities for D = 1m, C_D = 0.5

	Power (W/l)					
m	V_∞ = 1m/s	V_∞ = 2m/s	V_∞ = 4m/s	V_∞ = 6m/s	V_∞ = 8m/s	V_∞ = 10m/s
1	0.260	2.08	16.7	56.2	133.2	260.1
2	0.357	2.86	22.9	77.2	182.9	357.3
3	0.400	3.20	25.6	86.4	204.8	399.9
5	0.438	3.50	28.1	94.6	224.3	438.1
10	0.468	3.74	29.9	101.0	239.5	467.8

Table B2. C_p vs. m for series of freestream velocities for D = 1m, C_D = 0.5

	C_p					
m	V_∞ = 1m/s	V_∞ = 2m/s	V_∞ = 4m/s	V_∞ = 6m/s	V_∞ = 8m/s	V_∞ = 10m/s
1	0.425	0.4.25	0.425	0.425	0.425	0.425
2	0.583	0.583	0.583	0.583	0.583	0.583
3	0.653	0.653	0.653	0.653	0.643	0.653
5	0.716	0.715	0.715	0.715	0.715	0.715
10	0.764	0.764	0.764	0.764	0.764	0.754

B2: Comparisons for actuator cylinders of variable diameter

Table B3. Power vs. D for series of freestream velocities with C_D = 0.5, m = 1

	Power (W/l)				
D (m)	V_∞ = 2m/s	V_∞ = 4m/s	V_∞ = 6m/s	V_∞ = 8m/s	V_∞ = 10m/s
0.5	0.806	6.45	21.8	51.6	100.7
1	2.09	16.6	56.4	133.6	260.9
2	4.18	33.5	113.0	267.8	522.9
4	8.37	66.9	225.9	535.5	1045.9

Table B4. Power vs. D for series of freestream velocities with C_D = 0.5, m = 1 continued

	Power (W/l)				
D (m)	V_∞ = 12m/s	V_∞ = 15m/s	V_∞ = 18m/s	V_∞ = 21m/s	V_∞ = 24m/s
0.5	174.0	339.9	587.3	932.5	1392.0
1	450.8	880.5	1521.5	2416.1	3606.5
2	903.7	1765.0	3049.8	4843.1	7229.1
4	1807.3	3529.1	6099.5	9685.8	14458.1

Appendix C: Chapter 4 Figures and Data

C1: Power vs. spacing for variable m

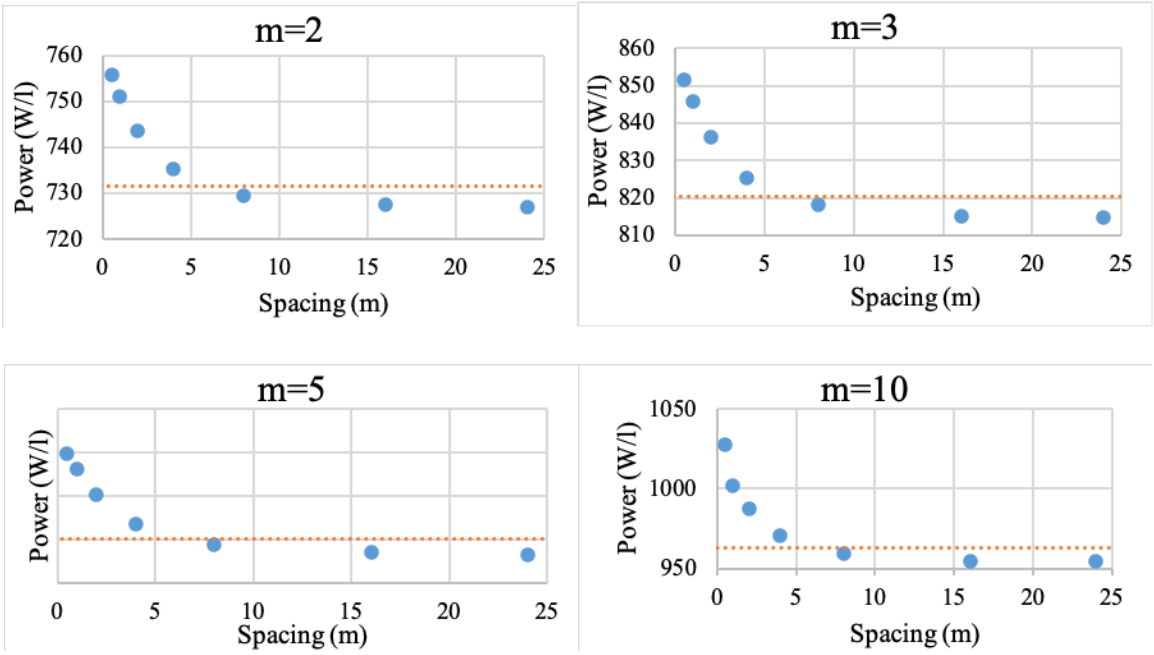

Figure C1. Power vs spacing for variable m

Table C1. Power vs. s for variable *m* with C_D = 0.5, *D* = 2m

	Power (W/l)					
Spacing (m)	*m* = 1	*m* = 2	*m* = 3	*m* = 5	*m* = 10	*m* = 20
0.5	542.9	755.8	851.7	939.6	1027.8	1046.4
1	540.4	751.0	845.6	932.1	1001.9	1036.1
2	536.6	743.7	836.2	920.3	987.4	1019.6
4	532.4	735.3	825.5	906.7	970.6	1000.3
8	529.4	729.5	818.0	897.3	959.0	987.1
16	528.4	727.4	815.2	893.9	954.8	982.3
24	528.2	727.0	814.8	893.1	954.1	981.5

Table C2. Power vs s for two VAWT refinement cases with m = 20

	s = 0.01m	s = 0.1m	s = 0.25m
Power (W/l)	1052.287	1050.603	1047.107

C2 Power vs. downfield distance for three VAWT arrays

Table C3. Power for each turbine in VAWT array for s = 0.5m.

	Power (W/l)							
x_{DF}	0m	0.5m	1m	1.5m	2m	2.5m	3m	3.5m
Front VAWT	1023.2	1026.4	1029.4	1029.3	1030.8	1034.5	1035.4	1036.4
Downfield VAWT	885.4	881.3	873.6	866.7	860.2	858.1	854.0	813.9
Total System Power	2931.8	2934.1	2932.3	2925.3	2921.8	2927.1	2924.7	2886.6

Table C4. Power for each turbine in VAWT array for s = 1.0m.

	Power (W/l)							
x_{DF}	0m	0.5m	1m	1.5m	2m	2.5m	3m	3.5m
Front VAWT	1018.0	1018.9	1020.7	1022.8	1024.0	1025.1	1026.3	1026.6
Downfield VAWT	1128.5	1129.2	1125.8	1121.2	1117.5	1114.6	1111.2	1109.0
Total System Power	3164.5	3166.9	3167.2	3166.8	3165.5	3164.8	3163.8	3162.2

Table C5. Power for each turbine in VAWT array for s = 2.0m.

	Power (W/l)							
x_{DF}	0m	0.5m	1m	1.5m	2m	2.5m	3m	3.5m
Front VAWT	1013.6	1010.2	1009.1	1009.0	1009.4	1010.0	1010.5	1011.0
Downfield VAWT	1225.1	1233.9	1230.0	1228.2	1222.4	1222.8	1214.5	1211.5
Total System Power	3252.4	3254.2	3248.3	3246.2	3241.2	3242.7	3235.5	3233.5

Table C6. Power for each turbine in VAWT array for s = 4.0m.

	Power (W/l)							
x_{DF}	0m	0.5m	1m	1.5m	2m	2.5m	3m	3.5m
Front VAWT	1007.8	1002.4	998.5	995.9	994.2	993.1	992.5	992.1
Downfield VAWT	1051.0	1056.9	1056.6	1055.5	1052.7	1051.2	1047.4	1045.2
Total System Power	3066.6	3061.7	3053.6	3047.3	3041.1	3037.4	3032.4	3029.4

Table C7. Power for each turbine in VAWT array for refinement case with s = 1.25m.

	Power (W/l)							
x_{DF}	0m	0.5m	1m	1.5m	2m	2.5m	3m	3.5m
Front VAWT	1019.8	1019.2	1020.1	1021.3	1022.5	1023.5	1024.2	1024.8
Downfield VAWT	1234.2	1233.5	1229.0	1223.6	1218.6	1215.6	1212.2	1211.4
Total System Power	3273.9	3271.9	3269.2	3266.3	3263.6	3262.5	3260.6	3260.9

Table C8. Power for each turbine in VAWT array for refinement case with *s* = 1.5m.

	Power (W/l)							
x_{DF}	0m	0.5m	1m	1.5m	2m	2.5m	3m	3.5m
Front VAWT	1018.5	1017.8	1017.6	1017.6	1018.5	1019.3	1020.0	1020.5
Downfield VAWT	1296.0	1287.2	1271.9	1270.9	1262.3	1260.0	1261.6	1252.6
Total System Power	3332.9	3322.8	3307.1	3306.1	3299.3	3298.7	3301.6	3293.7

Table C9. Power for each turbine in VAWT array for refinement case with s = 1.75m.

	Power (W/l)							
x_{DF}	0m	0.5m	1m	1.5m	2m	2.5m	3m	3.5m
Front VAWT	1017.4	1014.7	1014.0	1014.4	1015.0	1015.6	1016.2	1016.7
Downfield VAWT	1276.3	1306.5	1299.7	1277.8	1267.5	1259.7	1249.5	1249.7
Total System Power	3311.1	3335.9	3327.8	3306.5	3297.5	3290.9	3281.9	3283.1

Table C10. Power for each location in VAWT array for refinement case with *s* = 2.25m.

	Power (W/l)							
x_{DF}	0m	0.5m	1m	1.5m	2m	2.5m	3m	3.5m
Front VAWT	1015.8	1011.6	1009.7	1009.1	1009.1	1009.3	1009.7	1010.0
Downfield VAWT	1189.9	1196.7	1195.6	1191.8	1187.5	1183.5	1180.1	1177.4
Total System Power	3221.6	3219.9	3215.0	3209.9	3205.6	3202.2	3199.5	3197.5

Appendix D: Chapter 5 Figures and Data

Figure D1. Pressure contours for two VAWT array with D = 0.5m, C_D = 0.5, and V_∞ = 50m/s

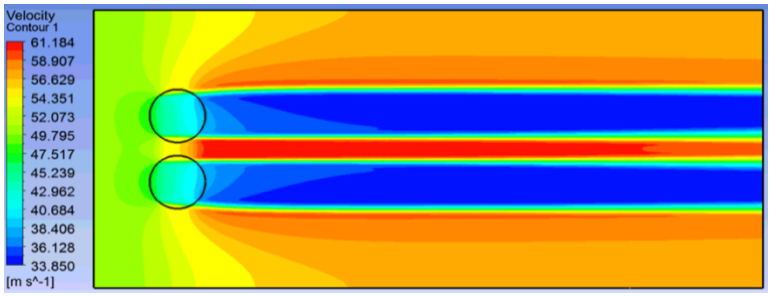

Figure D2. Velocity contours for two VAWT array with D = 0.5m, C_D = 0.5, and V_∞ = 50m/s

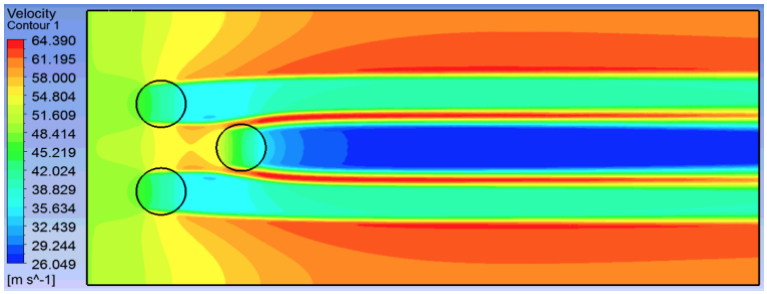

Figure D3. Velocity contours for three VAWT array with D = 0.5m, C_D = 0.5, and V_∞ = 50m/s

Table D1. Power for each location in two and three VAWT arrays

	Power (W)		
Freestream Velocity	V_∞ = 30m/s	V_∞ = 40m/s	V_∞ = 50m/s
Two VAWT	2106.7	4993.6	9753.1
Three VAWT Front	9519.4	4874.0	9519.4
Three VAWT Downfield	12170.9	6231.4	12170.9

Vita

Cory Schovanec

Degrees	**M.S. Aerospace Engineering**, Washington University in St. Louis, May 2020
	B.S. Mechanical Engineering, Washington University in St. Louis, May 2020
	B.A. Applied Physics, Southwestern University, May 2018
Professional Societies	Pi Beta Kappa Theta of Texas Chapter
Publications	Cory Schovanec and Ramesh Agarwal, "CFD Modeling of a Vertical Axis Wind Turbine using Actuator Cylinder Theory," 2020 AIAA Aviation Forum, June 2020